

Electronic Raman scattering in a multi-band model

Ivan Kupčić and Slaven Barišić

Department of Physics, Faculty of Science, POB 331, HR-10 002 Zagreb, Croatia

Charge-charge, current-current and Raman correlation functions are derived in a consistent way using the unified response theory. The theory is based on the precise description of the conduction electron coupling to the external electromagnetic fields, distinguishing further the direct and indirect (assisted) scattering on the inhomogeneities. The two scatterings are distinguished in terms of the energy and momentum conservation laws. The theory is illustrated on the Emery three-band model for the high- T_c materials with the incoherent electron scattering on impurities and coherent scattering on the static antiferromagnetic (AF) potential. It is shown, for the first time, that the incoherent indirect processes dominate the low-frequency part of the Raman spectra, while the long-range screening is playing a minor role. In the mid-infrared frequency range the coherent AF processes are dominant. In contrast to the nonresonant B_{1g} response, which is large by itself, the resonant interband transitions enhance both the A_{1g} and B_{1g} Raman spectra to comparable values, in good agreement with experimental observation. It is further argued that the AF correlations of the $d_{x^2-y^2}$ symmetry give rise to the mid-infrared peak in the B_{1g} Raman spectrum, accompanied by a similar peak in the optical conductivity. The doping behavior of these peaks is shown to be correlated with the linear doping dependence of the Hall number, as observed in all underdoped high- T_c compounds.

PACS numbers: 78.30.-j, 74.72.Dn, 74.25.Gz

Keywords: high- T_c superconductors, electronic band structure, long-range Coulomb screening, electronic Raman scattering, optical conductivity, Hall coefficient

I. INTRODUCTION

Resonant enhancement of the purely electronic Raman spectra or of the spectra corresponding to other Raman active modes [1] is characteristic of those high- T_c cuprates that exhibit substantial optical activity in the visible frequency region [2, 3]. Various more or less pronounced resonant features are observed in the measured Raman spectra, such as a strong dependence of the intensity of the B_{1g} two-magnon peak on the frequency of the incoming photon and on doping [3, 4, 5, 6]. Equally important are the relative intensities of the low-frequency Drude part of the Raman spectra and the anomalous frequency dependence of the associated Drude tail [3, 4, 7, 8, 9].

Actually, the experimental Raman studies took different directions. First, the investigations of the effects of the superconducting (SC) gap and pseudogap on the Drude part of the B_{2g} spectra of $\text{YBa}_2\text{Cu}_3\text{O}_{7-x}$ [7] and $\text{Bi}_2\text{Sr}_2\text{Ca}_1\text{Cu}_2\text{O}_{8+x}$ [10] confirmed the conclusions of other experiments [11, 12] that the superconducting gap with the magnitude of the order of 25 meV possesses predominantly the $d_{x^2-y^2}$ symmetry. Second, the B_{1g} spectra in $\text{La}_{2-x}\text{Sr}_x\text{CuO}_4$ [13] and $\text{Bi}_2\text{Sr}_2\text{Ca}_1\text{Cu}_2\text{O}_{8+x}$ [6] show, at temperatures up to room temperature, a strong two-magnon peak at 100–300 meV and a secondary structure at a frequency about three times lower. Both scales exhibit the same doping behavior. Similar scales appear in other experiments too, including measurements of the specific heat [12]. The smaller scale is usually associated with the characteristic antiferromagnetic (AF) energy [5, 6, 12, 13].

Caution with such assignment is, however, in order

because the normal-state band structure can also exhibit small energy scales, induced by strong charge correlations and related in particular to interband transitions [14]. Indeed, angle-resolved photoemission spectroscopy (ARPES) measurements of the conduction band in the “normal state” reveal small associated energy scales of the order of 100 meV or less [11, 15]. It is therefore important to distinguish between the small scales related to the charge correlations in the “normal-state” properties, the interband transitions in particular, and the correlation scales usually associated with excitations through the AF and SC gaps or pseudogaps in the “normal-state” band structure. The main purpose of the present paper is to discuss the existing Raman data from this point of view. This is accompanied here by the solution of several long-standing classical problems, concerning the electronic Raman scattering.

Following the simple Raman analysis given by Abrikosov and Genkin [16], the theoretical Raman investigations of the high- T_c cuprates usually neglect (e.g. Refs. [17, 18, 19, 20, 21, 22, 23, 24]) the resonant effects and replace the exact Raman vertex functions with the static ones in the description of the corresponding spectra. However, in the final stage of these calculations neither the static-Raman-vertex approximation (SRVA) has been used carefully, nor has its validity been examined. Actually, the Raman vertices in the static limit carry fundamental information on the position of the van Hove (vH) singularities in the electron dispersion through the Brillouin zone. These vertices enter, in an exact way, into the expressions for the DC conductivity, $\sigma_{\alpha\alpha}^{\text{DC}}$, and the Hall number, n_H , the majority of the anomalous features of which can be associated with the occurrence of the van Hove singularities close to the Fermi surface. It

is therefore appropriate to discuss the validity of SRVA for the Raman spectra, in relation to the properties that contain these vertices exactly (e.g. $\sigma_{\alpha\alpha}^{\text{DC}}$ and n_H).

In the present work, we shall first show that one has to go beyond the SRVA by taking the resonant intermediate processes into account to obtain the Drude spectral weight comparable for all three Raman polarizations (A_{1g} , B_{1g} , and B_{2g}), as usually found in experiments [5, 6, 7]. For this purpose, we shall use the elastic-Raman-vertex approximation (ERVA), which is a natural generalization of SRVA, and an extension to Raman scattering of the recent multiband optical conductivity analysis [25, 26].

Next we examine the role of the long-range Coulomb forces in the normal-state Raman response. The Raman active quadrupolar excitations of the electronic system induced by the electromagnetic field are coupled to the long-wavelength metallic charge redistribution. This coupling can lead to interesting screening effects [17, 18, 19, 20, 21, 22, 27, 28, 29, 30], which is currently the subject of several controversies and will be disentangled here.

Finally, the effects of the AF correlations on the spectral functions will be approximated in terms of an effective potential $\Delta(\mathbf{k})$ of $d_{x^2-y^2}$ symmetry [25, 31]. It will be shown that such a perturbation produces a maximum in the B_{1g} Raman channel at nearly the same energy as in the optical conductivity, while the low-lying B_{2g} spectrum remains unchanged. Finally, it will be argued that such a perturbation doubles the number of van Hove singularities, restoring the local electron-hole symmetry of the conduction band, as can be directly inferred by comparing the measured [2, 32] and calculated doping dependences of the Hall number in the electron-doped and hole-doped regimes.

In Sec. II the response of the electronic system to external transverse vector fields is formulated for a multiband model and applied to the Emery three-band model where the local field corrections are absent. The contributions of the direct and indirect electron-hole pair excitations to the Raman correlation functions are determined, including the screening by the multiband RPA (random phase approximation) dielectric function. The structure of the low-frequency (Drude) contribution to the Raman correlation functions is given in Secs. III and IV. The relation between the ERVA and SRVA is discussed in Sec. V. The predictions of the $\Delta(\mathbf{k}) \neq 0$ model for the Hall number, the optical conductivity, and the corresponding contributions to the B_{1g} and B_{2g} Raman spectra are given in Sec. VI, and compared to the experimental data. Sec. VII contains the concluding remarks.

II. MULTIBAND MODEL HAMILTONIAN

A. Emery three-band model

We consider the conduction electrons described by the reduced version of the quasi-two-dimensional Emery three-band model [33], in which the second-neighbor bond energy t_{pp} is set to zero, and the short-range interactions V_{pd} and V_{pp} are approximately included in the copper and oxygen site energies. t_{pp} , important in the behavior of the B_{2g} modes and in many other properties of the high- T_c cuprates, should not affect the A_{1g} and B_{1g} modes in a critical manner. The Hamiltonian is

$$H = H_0 + H'_1 + H'_2 + H^{\text{ext}}. \quad (1)$$

H_0 is the effective single-particle term. The electron scattering on impurities is described by H'_1 . $H'_2 = H_c + H_{\text{AF}}$ represents the two-particle interactions, including both the long-range Coulomb forces (H_c) and the residual interactions responsible for the AF correlations (H_{AF}). H^{ext} describes the coupling of the conduction electrons to the external fields.

Using the slave-boson approach to treat the limit of large Hubbard interaction on the copper site U_d , the effective single-particle Hamiltonian [34, 35] can be written in the representation of the delocalized atomic orbitals as

$$H_0 = \sum_{ll'\mathbf{k}\sigma} [H_0^{ll'}(\mathbf{k})l_{\mathbf{k}\sigma}^{\dagger}l_{\mathbf{k}\sigma}' + \text{H.c.}], \quad (2)$$

with the orbital index $l, l' = d, p_x, p_y$. Here the diagonal and off-diagonal matrix elements have the well-known form: $H_0^{ll}(\mathbf{k}) = E_l - 2t_{\perp} \cos k_z a_3$, $H_0^{dp_{\alpha}}(\mathbf{k}) = 2it_{\text{pd}} \sin \frac{1}{2}\mathbf{k} \cdot \mathbf{a}_{\alpha}$, with $\alpha = x, y$, and $H_0^{p_x p_y}(\mathbf{k}) = 0$ ($\mathbf{a}_1, \mathbf{a}_2$, and \mathbf{a}_3 are the primitive vectors of the tetragonal lattice in question). E_l are the renormalized site energies, t_{pd} is the renormalized first-neighbor bond-energy, and t_{\perp} is the interplane bond-energy. Using the transformations

$$l_{\mathbf{k}\sigma}^{\dagger} = \sum_L U_{\mathbf{k}}(l, L) L_{\mathbf{k}\sigma}^{\dagger}, \quad (3)$$

H_0 is diagonalized in terms of three bands [34]

$$H_0 = \sum_{L\mathbf{k}\sigma} E_L(\mathbf{k}) L_{\mathbf{k}\sigma}^{\dagger} L_{\mathbf{k}\sigma}, \quad (4)$$

with the band indices $L = c$ for the nearly half filled (conduction) bonding band and $L = N, P$ for the non-bonding and antibonding bands (which are empty in the hole picture used here). The structure of $E_L(\mathbf{k})$ and $U_{\mathbf{k}}(l, L)$ is well known [34, 36].

The effects of the AF correlations [37] on the excitation spectrum will be considered only for the processes within the conduction band $L = c$ which are modeled by

$$H_{\text{AF}} = \sum_{\mathbf{k}\sigma} [\Delta(\mathbf{k}) c_{\mathbf{k}\sigma}^{\dagger} c_{\mathbf{k}\pm\mathbf{Q}_{\text{AF}}\sigma} + \text{H.c.}]. \quad (5)$$

As is well known, for $t_{\text{pp}} = 0$, the AF wave vector \mathbf{Q}_{AF} is the ideal nesting vector of the half filled conduction band. Apparently, Eq. (5) can also describe dimerizations other than AF (spin-Peierls, charge-density waves).

The long-range forces are given by

$$H_c = \sum_{\mathbf{q} \neq 0} \frac{2\pi}{vq^2} \hat{q}(-\mathbf{q}) \hat{q}(\mathbf{q}), \quad (6)$$

with $\hat{q}(\mathbf{q})$ being the charge density operator,

$$\hat{q}(\mathbf{q}) = \sum_{LL'} \sum_{\mathbf{k}\sigma} eq^{LL'}(\mathbf{k}, \mathbf{k} + \mathbf{q}) L_{\mathbf{k}\sigma}^\dagger L'_{\mathbf{k}+\mathbf{q}\sigma}, \quad (7)$$

and the $q^{LL'}(\mathbf{k}, \mathbf{k} + \mathbf{q})$ are the related dimensionless intra- and interband charge vertices [see Appendix C and Eq. (12)]. On the other hand, in the single-particle scattering term H'_1 only the intraband impurity scattering processes are usually assumed to be important [38, 39]

$$H'_1 = \sum_{L\mathbf{k}\mathbf{k}'\sigma} V_1^{LL}(\mathbf{k} - \mathbf{k}') L_{\mathbf{k}\sigma}^\dagger L_{\mathbf{k}'\sigma}. \quad (8)$$

B. Electromagnetic coupling

The coupling of the conduction electrons to the electromagnetic fields polarized in the α and/or β direction is given by [25, 40, 41]

$$H^{\text{ext}} = H_1^{\text{ext}} + H_2^{\text{ext}} = -\frac{1}{c} \sum_{\mathbf{q}\alpha} A_\alpha(\mathbf{q}) \hat{J}_\alpha(-\mathbf{q}) - \frac{e^2}{2mc^2} \sum_{\mathbf{q}\mathbf{q}'\alpha\beta} A_\alpha(\mathbf{q} - \mathbf{q}') A_\beta(\mathbf{q}') \hat{\gamma}_{\alpha\beta}(-\mathbf{q}; 2). \quad (9)$$

Here

$$\begin{aligned} \hat{J}_\alpha(\mathbf{q}) &= \sum_{LL'} \sum_{\mathbf{k}\sigma} J_\alpha^{LL'}(\mathbf{k}) L_{\mathbf{k}\sigma}^\dagger L'_{\mathbf{k}+\mathbf{q}\sigma}, \\ \hat{\gamma}_{\alpha\beta}(\mathbf{q}; 2) &= \sum_{LL'} \sum_{\mathbf{k}\sigma} \gamma_{\alpha\beta}^{LL'}(\mathbf{k}; 2) L_{\mathbf{k}\sigma}^\dagger L'_{\mathbf{k}+\mathbf{q}\sigma}, \end{aligned} \quad (10)$$

are, respectively, the current density and bare Raman density operators [16, 25]. The explicit form of the current vertices, $J_\alpha^{LL'}(\mathbf{k})$, and the bare Raman vertices, $\gamma_{\alpha\beta}^{LL'}(\mathbf{k}; 2)$ for the $t_{\text{pp}} = 0$ Emery three-band model are given in Appendix A.

This coupling can be contrasted to the coupling to the external scalar fields $V^{\text{ext}}(\mathbf{q})$,

$$H^{\text{ext}} = \sum_{\mathbf{q}} V^{\text{ext}}(\mathbf{q}) \hat{q}(-\mathbf{q}), \quad (11)$$

used in the longitudinal response theory (see Appendix C). It is important to notice that, due to the absence of the local field corrections [42, 43] in the Emery model, the

long-wavelength charge vertices ($\mathbf{q} = \sum_\alpha q_\alpha \hat{e}_\alpha$ is small) satisfy the general relation [36, 44]

$$\begin{aligned} eq^{LL'}(\mathbf{k} + \mathbf{q}, \mathbf{k}) &\approx e\delta_{L,L'} \\ &+ (1 - \delta_{L,L'}) \sum_\alpha \frac{\hbar q_\alpha J_\alpha^{LL'}(\mathbf{k})}{E_{L'}(\mathbf{k} + \mathbf{q}) - E_L(\mathbf{k})}, \end{aligned} \quad (12)$$

with the longitudinal current vertices $J_\alpha^{LL'}(\mathbf{k})$ identical to the transverse current vertices given by Eqs. (10).

III. RAMAN CORRELATION FUNCTIONS IN PURE SYSTEMS

In the mean-field slave-boson theory the physical Raman correlation functions are proportional to the corresponding correlation functions of the auxiliary fermions described by the band structure associated with Eqs. (4) and (5). The simplest operative way to determine the Raman correlation functions of this three-band auxiliary fermion model is to consider the Goldstone theorem for the thermodynamic potential in the Matsubara representation with $H' = H^{\text{ext}} + H'_2 + H'_1$ representing the perturbation, and collect all fourth-order contributions in the vector fields $A_\alpha(\mathbf{q}')$ and $A_\beta(\mathbf{q}')$. It is convenient to divide this procedure into four steps. First, the $H' = H^{\text{ext}}$ case provides the definition of the Raman vertex functions in the multiband model under consideration, with particular care devoted to the resonant enhancement of the Raman scattering processes. Second, for $H' = H^{\text{ext}} + H_c$, we shall define the direct contributions to the Raman correlation functions and reconsider the role of the long-range screening in the pure multiband models. Third, by considering the perturbation $H' = H^{\text{ext}} + H_c + H'_1$, we shall introduce the distinction between the direct and indirect (impurity-assisted) electron-hole excitations and discuss which of these processes dominate the Raman spectra measured in the high- T_c cuprates. Finally, by including H_{AF} , we shall study the influence of the low-frequency excitations across the AF (pseudo)gap on both the Drude part and the related low-lying interband part of the Raman spectrum.

A. Raman vertex functions in pure systems

In the absence of impurities and AF scattering processes, the direct summation of the fourth-order diagrams in the vector fields $A_\alpha(\mathbf{q}')$ and $A_\beta(\mathbf{q}')$ leads to Fig. 1(a), representing the Raman correlation function in the ideal lattice, approximately given by its intraband contribution. Namely, in the high- T_c cuprates, the interband excitation energies are of the order of typical optical energies, 1.75–2.75 eV, which is far above the largest Raman shift (defined below) measured in experiments. Consequently, the interband contributions to the Raman correlation functions can safely be neglected in the ideal lattice. As will be seen below, the AF correlations introduce

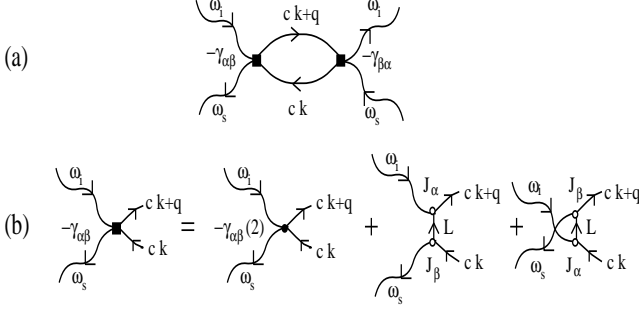


FIG. 1: (a) The purely electronic intraband Raman correlation functions in a pure system. (b) The Raman vertex (black square) shown in terms of the bare Raman vertex (black circle) and the interband current vertices (open circles).

the possibility of the low-lying “interband” excitations requiring the generalization (Sec. III B) of Fig. 1(a).

Thus, in a pure system (denoted by p) we have

$$\begin{aligned} \chi_{\alpha\beta,\beta\alpha}^p(\mathbf{q}, \omega, \omega_i) &\approx \frac{1}{v} \sum_{\mathbf{k}\mathbf{k}'\sigma} \gamma_{\alpha\beta}^{cc}(\mathbf{k}, \omega_i, \omega_s) \\ &\times \frac{1}{\hbar} \mathcal{D}_p^{cc}(\mathbf{k}, \mathbf{k}_+, \mathbf{k}'_+, \mathbf{k}', \omega) \gamma_{\beta\alpha}^{cc}(\mathbf{k}', \omega_s, \omega_i), \end{aligned} \quad (13)$$

where $\mathcal{D}_p^{cc}(\mathbf{k}, \mathbf{k}_+, \mathbf{k}'_+, \mathbf{k}', \omega)$ is the intraband electron-hole propagator in the ideal lattice, defined by

$$\begin{aligned} \frac{1}{\hbar} \mathcal{D}_p^{LL'}(\mathbf{k}, \mathbf{k}_+, \mathbf{k}'_+, \mathbf{k}', \omega) \\ = \delta_{\mathbf{k}, \mathbf{k}'} \frac{f_L(\mathbf{k}) - f_{L'}(\mathbf{k} + \mathbf{q})}{\hbar\omega + E_L(\mathbf{k}) - E_{L'}(\mathbf{k} + \mathbf{q}) + i\eta}, \end{aligned} \quad (14)$$

for the band indices $L = L' = c$. $f_L(\mathbf{k}) \equiv f(E_L(\mathbf{k}))$ is the Fermi-Dirac distribution function. Furthermore, the $\gamma_{\alpha\beta}^{cc}(\mathbf{k}, \omega_i, \omega_s)$ are the related intraband Raman vertices

$$\begin{aligned} \gamma_{\alpha\beta}^{cc}(\mathbf{k}, \omega_i, \omega_s) &= -\frac{m}{e^2} \sum_{L \neq c} \left[\frac{J_\alpha^{Lc}(\mathbf{k}) J_\beta^{cL}(\mathbf{k})}{\hbar\omega_i - E_{Lc}(\mathbf{k}) + i\eta} \right. \\ &\left. - \frac{J_\alpha^{cL}(\mathbf{k}) J_\beta^{Lc}(\mathbf{k})}{\hbar\omega_s + E_{Lc}(\mathbf{k}) + i\eta} \right] + \gamma_{\alpha\beta}^{cc}(\mathbf{k}; 2), \end{aligned} \quad (15)$$

and $\mathbf{k}_+ = \mathbf{k} + \mathbf{q}$. Here ω_i, \mathbf{q}'' , α and ω_s, \mathbf{q}' , β are the frequencies, wave vectors and polarization indices of the incoming and scattered photons, respectively. $\omega = \omega_i - \omega_s$ is the Raman shift, $\mathbf{q} = \mathbf{q}'' - \mathbf{q}'$, and $E_{LL'}(\mathbf{k}) = E_L(\mathbf{k}) - E_{L'}(\mathbf{k})$. As mentioned at the beginning of this section, both the impurity scattering processes and the AF correlations are absent in $\gamma_{\alpha\beta}^{cc}(\mathbf{k}, \omega_i, \omega_s)$.

The diagrammatic representation of the Raman vertices is shown in Fig. 1(b). The first term on the right-hand side is the quadratic coupling term, while the latter two represent the bi-linear contributions. The resonant nature of the Raman scattering processes refers to the bi-linear terms. The resonant effects are large in the high- T_c cuprates because, as mentioned above, the interband excitation energies $E_{Lc}(\mathbf{k})$ in Eq. (15) are of the

order of typical optical energies. In addition to the resonant condition, $E_{Lc}(\mathbf{k}) \approx \hbar\omega_i$ and/or $E_{Lc}(\mathbf{k}) \approx \hbar\omega_s$, the efficiency of the resonant enhancement of the Raman scattering processes depends also on the relaxation processes in the intermediate interband photon absorptions/emissions that are omitted here. Although, in principle, these relaxation processes have to be treated on an equal footing with the relaxation processes in the electron-hole propagators $\mathcal{D}^{LL'}(\mathbf{k}, \mathbf{k}_+, \mathbf{k}'_+, \mathbf{k}', \omega)$, we shall use below an approximate treatment, by including the former phenomenologically (see Sec. III A.2) and the latter by using the direct summation method (Sec. IV).

1. Effective mass theorem

Let us consider the $\omega_i = \omega_s = 0$, $\eta \rightarrow 0$ limit of Eq. (15). The result is the static Raman vertex of the form

$$\gamma_{\alpha\beta}^{cc}(\mathbf{k}) = \gamma_{\alpha\beta}^{cc}(\mathbf{k}; 2) + \frac{m}{e^2} \sum_{L \neq c} \frac{2J_\alpha^{Lc}(\mathbf{k}) J_\beta^{cL}(\mathbf{k})}{E_{Lc}(\mathbf{k})}. \quad (16)$$

Here the symmetry relation $J_\alpha^{Lc}(\mathbf{k}) = J_\alpha^{cL}(\mathbf{k})$ has been used. This expression can be combined with the relation

$$\gamma_{\alpha\beta}^{cc}(\mathbf{k}) = \mp \frac{m}{\hbar^2} \frac{\partial^2 E_c(\mathbf{k})}{\partial k_\alpha \partial k_\beta}$$

to obtain the “effective mass” theorem

$$\begin{aligned} \mp \frac{m}{\hbar^2} \frac{\partial^2 E_c(\mathbf{k})}{\partial k_\alpha \partial k_\beta} &= \gamma_{\alpha\beta}^{cc}(\mathbf{k}; 2) \\ &+ \frac{m}{e^2} \sum_{L \neq c} \frac{2J_\alpha^{Lc}(\mathbf{k}) J_\beta^{cL}(\mathbf{k})}{E_{Lc}(\mathbf{k})}. \end{aligned} \quad (17)$$

Eq. (17) [and Eq. (19)] holds even when its left-hand side is dependent on \mathbf{k} , i.e. beyond the effective mass approximation. The result is appropriate for any multiband model with the hole-like (– sign, the case considered here) or electron-like (+ sign) dispersion of the conduction electrons. This theorem turns out to be important to both the conductivity-sum-rule analyses [25] and the transport-coefficient studies, in particular when the system undergoes the AF phase transition, i.e. the term (5) is included.

The theorem states that the zero-frequency electron-hole pairs (corresponding to the formal limit $\omega_i, \omega_s \rightarrow 0$) can be excited by the electromagnetic fields through the bare quadratic electron-photon coupling and/or through the bi-linear term in which the first-order (high-frequency) interband excitations appear as virtual intermediate states.

2. Elastic-Raman-vertex approximation

Since the Raman shift $\omega = \omega_i - \omega_s$ is small in comparison with the typical values of ω_i or ω_s , it is reasonable,

in the numerical calculation in Sec. V, to use the elastic-Raman-vertex approximation

$$\gamma_{\alpha\beta}^{cc}(\mathbf{k}, \omega_i, \omega_s) \approx \gamma_{\alpha\beta}^{cc}(\mathbf{k}, \omega_i, \omega_i) \equiv \gamma_{\alpha\beta}^{cc}(\mathbf{k}, \omega_i), \quad (18)$$

in which the zero-frequency processes ($\omega_i, \omega_s \approx 0$) are approximately separated from the higher-frequency absorption/emission processes. The phenomenological treatment of the interband relaxation processes in the resonant channel then gives rise to the general expression

$$\begin{aligned} \gamma_{\alpha\beta}^{cc}(\mathbf{k}, \omega_i) &= \gamma_{\alpha\beta}^{cc}(\mathbf{k}) - \frac{m}{e^2} \sum_{L \neq c} \frac{(\hbar\omega_i)^2 J_{\alpha}^{Lc}(\mathbf{k}) J_{\beta}^{cL}(\mathbf{k})}{E_{Lc}^2(\mathbf{k})} \\ &\times \frac{2E_{Lc}(\mathbf{k})}{(\hbar\omega_i + i\hbar\Gamma_{\text{inter}})^2 - E_{Lc}^2(\mathbf{k})} \end{aligned} \quad (19)$$

[again $J_{\alpha}^{Lc}(\mathbf{k}) = J_{\alpha}^{cL}(\mathbf{k})$ is used].

It is useful now to incorporate the symmetry properties of the Emery three-band model into Eqs. (15) and (19). First, we remember that the analysis of the electronic Raman spectra of the high- T_c cuprates is usually focused on the in-plane polarization of the electromagnetic fields ($\alpha, \beta = x, y$). It is thus convenient to arrange the Raman vertices according to the irreducible representations of the D_{4h} point group [20, 28, 45]. The resulting Raman vertices are of the form $\gamma_{\nu}^{cc}(\mathbf{k}, \omega_i)$, with the label $\nu = A_{1g}, B_{1g}$, and B_{2g} representing the A_{1g} , B_{1g} , and B_{2g} Raman channels, respectively. The symmetrized vertices are

$$\begin{aligned} \gamma_{A_{1g}}^{cc}(\mathbf{k}, \omega_i) &= \gamma_{xx}^{cc}(\mathbf{k}, \omega_i) + \gamma_{yy}^{cc}(\mathbf{k}, \omega_i), \\ \gamma_{B_{1g}}^{cc}(\mathbf{k}, \omega_i) &= \gamma_{xx}^{cc}(\mathbf{k}, \omega_i) - \gamma_{yy}^{cc}(\mathbf{k}, \omega_i), \\ \gamma_{B_{2g}}^{cc}(\mathbf{k}, \omega_i) &= \gamma_{xy}^{cc}(\mathbf{k}, \omega_i). \end{aligned} \quad (20)$$

It should be noticed here that the Raman correlation functions of the tetragonal high- T_c cuprates are diagonal in this representation. The orthorhombic distortion of the CuO_2 plane, which occurs in some compounds ($\text{YBa}_2\text{Cu}_3\text{O}_{7-x}$, for example), mixes these three channels. However, as previously estimated [36], the mixing is typically of the order of 1/10 and is neglected in the present analysis.

B. Long-range screening in pure systems

The effects of the long-range Coulomb forces on the Raman correlation functions are given in the usual way [18, 19, 22, 27, 29, 30, 36]. In absence of the incoherent scattering processes those functions are described by the diagrams in Fig. 2(b). The screened correlation function $\tilde{\chi}_{\nu,\nu}(\mathbf{q}, \omega, \omega_i)$ is given by

$$\begin{aligned} \tilde{\chi}_{\nu,\nu}(\mathbf{q}, \omega, \omega_i) &= \chi_{\nu,\nu}(\mathbf{q}, \omega, \omega_i) \\ &+ \chi_{\nu,1}(\mathbf{q}, \omega, \omega_i) \frac{4\pi e^2}{q^2 \varepsilon(\mathbf{q}, \omega)} \chi_{1,\nu}(\mathbf{q}, \omega, \omega_i). \end{aligned} \quad (21)$$

The coupling function $\chi_{\nu,1}(\mathbf{q}, \omega, \omega_i)$ is defined by Eq. (13), with $\gamma_{\alpha\beta}^{cc}(\mathbf{k}, \omega_i) \gamma_{\beta\alpha}^{cc}(\mathbf{k}', \omega_i)$ replaced by

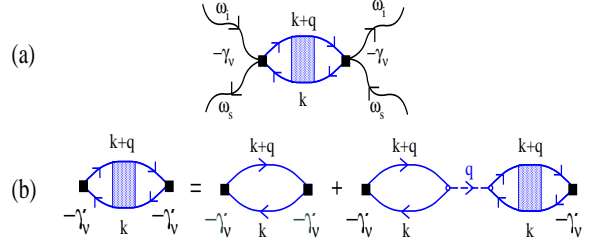


FIG. 2: (a) The Raman correlation functions in a general case with the long-range forces and the impurity scattering processes taken into account. The full rectangle is the Raman vertex of Fig. 1(b). The shaded box includes the electron-hole self-energy contributions associated with both the long-range forces and the impurity scattering processes. (b) The long-range screening of the Raman correlation functions in the case where the impurity scattering processes are absent. The open circles represent the charge vertices and the dashed line is the long-range force $4\pi e^2/q^2$.

$\gamma_{\nu}^{cc}(\mathbf{k}, \omega_i) q^{cc}(\mathbf{k}' + \mathbf{q}, \mathbf{k}')$. The dielectric function in Eq. (21) has the form

$$\varepsilon(\mathbf{q}, \omega) = \varepsilon_{\infty}(\mathbf{q}, \omega) - \frac{4\pi e^2}{q^2} \chi_{1,1}(\mathbf{q}, \omega), \quad (22)$$

with $e^2 \chi_{1,1}(\mathbf{q}, \omega)$ representing the charge-charge correlation function given by

$$\begin{aligned} e^2 \chi_{1,1}(\mathbf{q}, \omega) &= \frac{1}{v} \sum_{LL'} \sum_{\mathbf{k}\mathbf{k}'\sigma} e^2 q^{LL'}(\mathbf{k}, \mathbf{k} + \mathbf{q}) \\ &\times q^{L'L}(\mathbf{k}' + \mathbf{q}, \mathbf{k}') \frac{1}{\hbar} \mathcal{D}^{LL'}(\mathbf{k}, \mathbf{k}_+, \mathbf{k}'_+, \mathbf{k}', \omega). \end{aligned} \quad (23)$$

Here $\mathcal{D}^{LL'}(\mathbf{k}, \mathbf{k}_+, \mathbf{k}'_+, \mathbf{k}', \omega)$ is the electron-hole propagator defined in Appendix C.

For the B_{1g} and B_{2g} Raman channels, the coupling functions $\chi_{\nu,1}(\mathbf{q}, \omega, \omega_i)$ vanish for symmetry reasons, and the long-range forces do not affect the Raman spectra in the B_{1g} and B_{2g} channels. Furthermore, it is useful to separate the constant term in the A_{1g} Raman vertex from the dispersive term, $\gamma_{A_{1g}}^{cc}(\mathbf{k}, \omega_i) = \bar{\gamma}_{A_{1g}}^{cc}(\omega_i) + \hat{\gamma}_{A_{1g}}^{cc}(\mathbf{k}, \omega_i)$, in the way that $\hat{\chi}_{A_{1g},1}(\mathbf{q}, \omega, \omega_i) = 0$ [notice that $\gamma_{\nu}^{cc}(\mathbf{k}, \omega_i) = \hat{\gamma}_{\nu}^{cc}(\mathbf{k}, \omega_i)$ for $\nu = B_{1g}, B_{2g}$]. In this way $\hat{\chi}_{\nu,1}(\mathbf{q}, \omega, \omega_i) = 0$ for all three Raman channels. [The hat in $\hat{\chi}_{\nu,1}(\mathbf{q}, \omega, \omega_i)$ indicates that only the dispersive part of the vertex $\gamma_{\nu}^{cc}(\mathbf{k}, \omega_i)$, $\hat{\gamma}_{\nu}^{cc}(\mathbf{k}, \omega_i)$, is included in $\chi_{\nu,1}(\mathbf{q}, \omega, \omega_i)$.] Consequently, the dispersive terms $\hat{\gamma}_{\nu}^{cc}(\mathbf{k}, \omega_i)$ are unaffected by the long-range screening, at least in pure systems, while the constant term $\bar{\gamma}_{A_{1g}}^{cc}(\omega_i)$ is screened in the same way as the monopole charge $q^{cc}(\mathbf{k}, \mathbf{k} + \mathbf{q}) \approx 1$ [39, 40, 55].

The Raman spectra, associated with imaginary part of Eq. (21), comprise the incoherent electron-hole contributions characterized by the cut-off frequency of the order of qv_F and, for the A_{1g} channel, by the plasmon contribution related to the screening of $\bar{\gamma}_{A_{1g}}^{cc}(\omega_i)$. These spectra are directly related to the dynamical structure

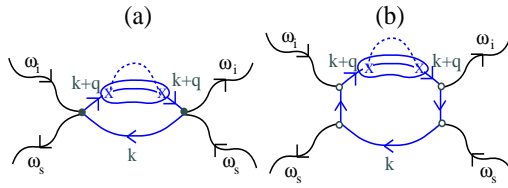


FIG. 3: Two typical direct Raman scattering processes proportional to $(H'_1)^2$. The self-energy parts on the diagrams that are treated as constant are encircled [26]. The crosses represent the impurity scattering H'_1 .

factor $S(\mathbf{q}, \omega) = -\text{Im}\{\tilde{\chi}_{1,1}(\mathbf{q}, \omega)\}$. The intensity of both the collective and incoherent electron-hole contributions to $-\text{Im}\{\tilde{\chi}_{\nu,\nu}(\mathbf{q}, \omega, \omega_i)\}$ is proportional to small q^2 . These types of signals have never been detected in the high- T_c cuprates [2, 19], in contrast to the semiconducting systems, such as GaAs ($q\nu_F \approx 50 \text{ cm}^{-1}$) [56]. In the high- T_c cuprates, the measured Raman spectra are roughly proportional to the optical conductivity, with the intensity proportional to the channel-dependent relaxation rates. This leads us to study the relaxation through impurity scattering.

IV. RAMAN CORRELATION FUNCTIONS IN SYSTEMS WITH DISORDER

A. Incoherent scattering

This section deals with the contributions of the incoherent scattering to the Raman correlation functions $\tilde{\chi}_{\nu,\nu}(\mathbf{q}, \omega, \omega_i)$, including the Coulomb screening effects. The discussion starts from the low order impurity scattering, continues by the summations to high orders and adds the Coulomb screening at the end. In this discussion it is convenient to distinguish between the direct and indirect processes, as further explained below.

1. Direct processes

As illustrated in Fig. 3, for all correlation functions considered in this article (charge-charge, current-current and Raman correlation functions), the probability for the direct electron-hole pair creation is proportional to $f_c(\mathbf{k}) - f_c(\mathbf{k}+\mathbf{q})$ and associated with the resonance condition $\hbar\omega \approx E_c(\mathbf{k}) - E_c(\mathbf{k}+\mathbf{q})$. The corresponding scattering paths $1 \rightarrow 3$ and $1 \rightarrow 2 \rightarrow 3$ are shown in Fig. 4. The direct impurity scattering can be roughly incorporated in the correlation functions in the standard phenomenological way [55]. Alternatively, one can apply the gauge-invariant treatment to sum the direct processes shown in Fig. 5 in powers of $(H'_1)^2$. The gauge invariance conserves the number of charge carriers in the scattering processes [40]. As shown in Appendix C, the latter approach gives the unscreened, direct charge-charge correlation function

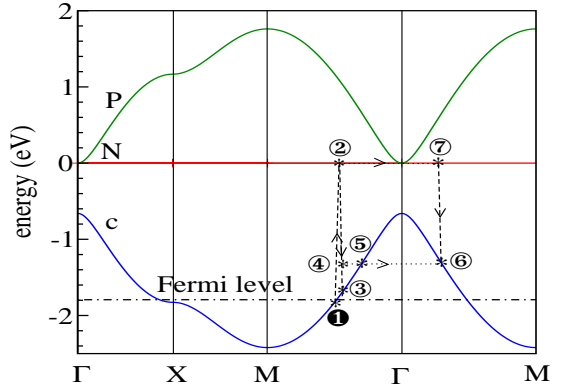


FIG. 4: The direct ($1 \rightarrow 2 \rightarrow 3$) and indirect (forward, $1 \rightarrow 2 \rightarrow 4 \rightarrow 5$, or backward, $1 \rightarrow 2 \rightarrow 4 \rightarrow 6$) intraband Raman scattering processes in the bi-linear channel. The solid lines represent the three bands of auxiliary fermions (the indices c , P and N) for the typical values of the model parameters $\Delta_{pd} = 0.66 \text{ eV}$ and $t_{pd} = 0.73 \text{ eV}$ [25, 50]. The energies are measured with respect to the energy of the $2p_\sigma$ oxygen orbitals, so that the dispersionless nonbonding band is placed at $E_p = 0$. The dashed lines are the photon dispersions, and the dot-dashed line is the Fermi energy $\mu = -1.793 \text{ eV}$ corresponding to the hole doping $\delta = 0.1$.

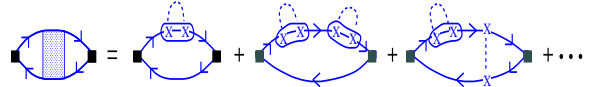


FIG. 5: A few direct contributions to the Raman correlation functions in powers of $(H'_1)^2$, according to Eqs. (C9), (C8) and (C4). The full rectangle is the effective Raman vertex of Fig. 1(b).

(intra- and interband contributions) of the form

$$e^2 \chi_{1,1}^d(\mathbf{q}, \omega) = \frac{1}{v} \sum_{\alpha'LL'k\sigma} \frac{q_{\alpha'}^2}{\omega^2} \left(\frac{\hbar\omega}{E_{L'L}(\mathbf{k}_+, \mathbf{k})} \right)^{n_{LL'}} |J_{\alpha'}^{LL'}(\mathbf{k})|^2 \times \frac{f_L(\mathbf{k}) - f_{L'}(\mathbf{k}_+)}{\hbar\omega + i\hbar\Gamma_{\alpha'}^{LL'}(\mathbf{k}, \omega) + E_{LL'}(\mathbf{k}, \mathbf{k}) - \frac{E_{L'L'}^2(\mathbf{k}, \mathbf{k}_+)}{\hbar\omega}}, \quad (24)$$

where $\mathbf{q} = \sum_{\alpha'} q_{\alpha'} \hat{e}_{\alpha'}$, $n_{LL} = 1$, $n_{LL'} = 2$, $\Gamma_{\alpha'}^{LL'}(\mathbf{k}, \omega) = \text{Im}\{\Sigma_{\alpha'}^{LL'}(\mathbf{k}, \omega)\}$ and $E_{LL'}(\mathbf{k}, \mathbf{k}_+) = E_L(\mathbf{k}) - E_{L'}(\mathbf{k}_+)$.

Eq. (24) can be easily generalized to other correlation functions. For the impurity scattering $\text{Im}\{\Sigma^{cc}(\mathbf{k}, \omega)\} \approx \Gamma_i^{c,d}$ (here, the index $i = 1, \alpha$, and ν for the charge, current, and Raman vertices, respectively). In the dynamical limit, we thus obtain the universal expression for the unscreened, direct intraband correlation functions

$$\chi_{i,j}^d(\mathbf{q}, \omega) = \sum_{\alpha'} \frac{q_{\alpha'}^2}{\omega} \frac{1}{\omega + i\Gamma_i^{c,d}} \frac{(at_{pd})^2}{v_0 \hbar^2} n_{i,j}^d(\mu). \quad (25)$$

Here $n_{i,j}^d(\mu)$ is the effective density of states at the Fermi

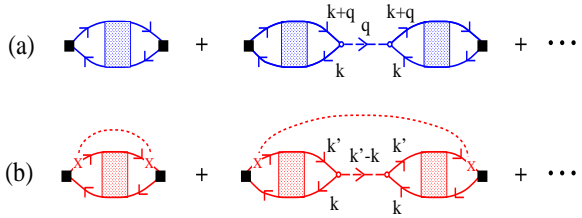


FIG. 6: The Coulomb screening of the direct (a) and indirect (b) processes in the Raman response functions in presence of the impurity scattering. Fig. (b) represents the quadrupolar analog of the well-known Hopfield series [39]. The dotted box includes the electron-hole self-energy contributions associated with the impurity scattering processes.

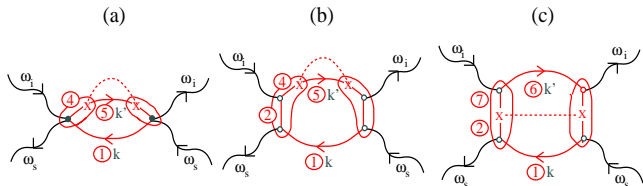


FIG. 7: Three typical indirect Raman scattering processes proportional to $(H'_1)^2$. The first two include the incoherent scattering of conduction electrons while the third shows the incoherent scattering in the empty band(s) (the notation is the same as in Fig. 4). The effective vertices are encircled [26].

energy given by

$$n_{1,1}^d(\mu) = -\frac{1}{N} \sum_{\mathbf{k}\sigma} |q^{cc}(\mathbf{k}, \mathbf{k} + \mathbf{q}) j_{\alpha'}^{cc}(\mathbf{k})|^2 \frac{\partial f_c(\mathbf{k})}{\partial E_c(\mathbf{k})}, \quad (26)$$

while $n_{\alpha,\alpha}^d(\mu)$, $n_{\nu,\nu}^d(\mu)$ and $n_{\nu,1}^d(\mu)$ are obtained by replacing $|q^{cc}(\mathbf{k}, \mathbf{k} + \mathbf{q})|^2 = 1$ in Eq. (26) with $(j_{\alpha}^{cc}(\mathbf{k}))^2$, $|\gamma_{\nu}^{cc}(\mathbf{k}, \omega_i)|^2$, and $\gamma_{\nu}^{cc}(\mathbf{k}, \omega_i) q^{cc}(\mathbf{k} + \mathbf{q}, \mathbf{k})$, respectively. Finally, $j_{\alpha}^{cc}(\mathbf{k}) = \hbar J_{\alpha}^{cc}(\mathbf{k}) / (e a t_{pd})$ is the dimensionless current vertex, Eq. (A5), and v_0 is the unit cell volume. For the electromagnetic fields ($i = \alpha, \nu$) the wave vector $\mathbf{q} = \sum_{\alpha'} q_{\alpha'} \hat{e}_{\alpha'}$ is perpendicular to the polarization of the fields; i.e. $q_{\alpha'} = q_z$ for the symmetrized Raman vertices in Eq. (20).

The RPA series for the screened direct contribution to the Raman correlation functions is illustrated in Fig. 6(a), and is given by inserting the expression (25) into Eq. (21). As can be easily seen, the intensity of both the plasmon and electron-hole incoherent contributions to $-\text{Im}\{\tilde{\chi}_{\nu,\nu}^d(\mathbf{q}, \omega, \omega_i)\}$ remains proportional to small q^2 .

2. Indirect processes

Omitting again the Coulomb screening to begin with, the impurity-assisted, indirect electron-hole contribution is associated to $f_c(\mathbf{k}) - f_c(\mathbf{k}')$, with uncorrelated \mathbf{k} and

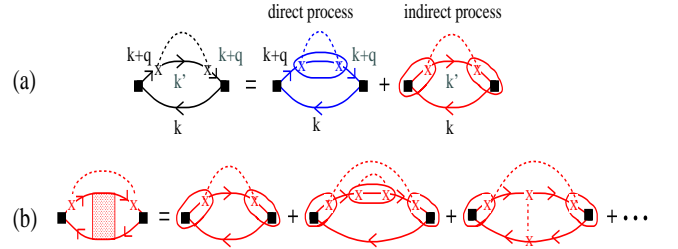


FIG. 8: (a) The direct and indirect high-frequency contributions [proportional to $(H'_1)^2$] to the Raman correlation functions [Fig. 3 and Fig. 7(a,b)]. (b) A few indirect leading terms in powers of $(H'_1)^2$.

\mathbf{k}' [see the $1 \rightarrow 4 \rightarrow 5$ processes shown in Fig. 4 and the related diagrams in Fig. 7(a), as well as the $1 \rightarrow 2 \rightarrow 4 \rightarrow 5$ processes represented by the diagram in Fig. 7(b)]. These types of processes become important when $\hbar\omega \gg |E_c(\mathbf{k}) - E_c(\mathbf{k} + \mathbf{q})|$, with the resonance at $\hbar\omega \approx E_c(\mathbf{k}) - E_c(\mathbf{k}')$. This is a typical situation encountered in the absorption and/or emission of photons by conduction electrons, i.e. in the intraband optical-conductivity and Raman experiments on metals. On the other hand, the indirect Raman scattering processes $1 \rightarrow 2 \rightarrow 7 \rightarrow 6$, shown in Fig. 7(c), are directly related to the indirect interband optical conductivity [55]. For the time-dependent H'_1 they are essential for the Raman analysis of the insulating and semiconducting systems [1]. In the present case, H'_1 includes only the impurity scattering and therefore the diagram in Fig. 7(c) has the resonant behavior similar to the diagram in Fig. 7(b). Thus the processes in Fig. 7(c) can be included in the effective Raman vertex (19) and will not be discussed hereafter.

The direct and indirect scattering processes, shown in Fig. 8(a), are large in the high-frequency limit [$\propto (H'_1)^2$]. The first qualitatively important corrections to the indirect high-frequency term come from the second and third term in Fig. 8(b) which are proportional to $(H'_1)^4/\omega$, i.e. they are singular in the zero-frequency limit. The consistent treatment of the indirect Raman scattering processes requires thus the summation to infinity of the most singular terms in powers of $(H'_1)^2/\omega$. This requires summing the singular contributions to all orders in $(H'_1)^2/\omega$ in order to obtain the description which is correct in both the high- and low-frequency limits.

As explained in Ref. [26] in the example of optical conductivity, the gauge-invariant treatment of the single-particle self-energy and vertex corrections in the indirect processes gives rise to effective vertices in which there is a complete cancellation of the scattering processes associated with the constant terms in the bare vertices. In the case of optical conductivity, this means that the indirect processes in the charge-charge correlation functions are absent altogether because the effective vertex $[q^{cc}(\mathbf{k}, \mathbf{k}) - q^{cc}(\mathbf{k}', \mathbf{k}')]/V_1^{cc}(\mathbf{k} - \mathbf{k}')/(\hbar\omega)$ vanishes due to the fact that $q^{cc}(\mathbf{k}, \mathbf{k}) \approx 1$. In the Raman case, the ef-

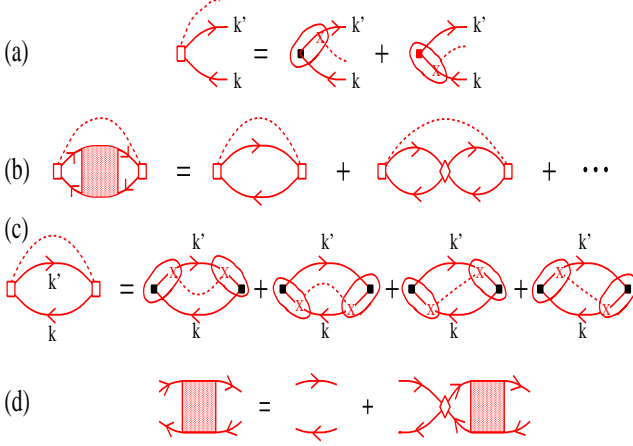


FIG. 9: (a) The effective Raman vertex (open square) in the indirect processes, $[\hat{\gamma}_\nu^{cc}(\mathbf{k}, \omega_i) - \hat{\gamma}_\nu^{cc}(\mathbf{k}', \omega_i)]V_1^{cc}(\mathbf{k} - \mathbf{k}')/(\hbar\omega)$. (b) The expansion of the indirect contribution to the Raman correlation functions in powers of $(H'_1)^2/\omega$, with the leading term explicitly shown in (c). The shaded box is the electron-hole propagator which is obtained by the self-consistent solution of the equation shown in (d) [26]. The diamond is the electron-hole self-energy containing both the single-particle self-energy and vertex corrections.

fective vertices $[\hat{\gamma}_\nu^{cc}(\mathbf{k}, \omega_i) - \hat{\gamma}_\nu^{cc}(\mathbf{k}', \omega_i)]V_1^{cc}(\mathbf{k} - \mathbf{k}')/(\hbar\omega)$ in $\chi_{\nu,\nu}^{\text{id}}(\omega, \omega_i)$ are given by the sum of two terms shown in Fig. 9(a), setting $\gamma_\nu^{cc}(\mathbf{k}, \omega_i) = \bar{\gamma}_\nu^{cc}(\omega_i) + \hat{\gamma}_\nu^{cc}(\mathbf{k}, \omega_i)$, and reduce to $[\hat{\gamma}_\nu^{cc}(\mathbf{k}, \omega_i) - \hat{\gamma}_\nu^{cc}(\mathbf{k}', \omega_i)]V_1^{cc}(\mathbf{k} - \mathbf{k}')/(\hbar\omega)$. The contribution to $\chi_{\nu,\nu}^{\text{id}}(\omega, \omega_i)$ of the constant terms $\bar{\gamma}_\nu^{cc}(\omega_i)$, present only in the $\nu = A_{1g}$ channel, thus vanishes, in analogy with the case of optical conductivity. In this way, $\chi_{\nu,\nu}^{\text{id}}(\omega, \omega_i) = \hat{\chi}_{\nu,\nu}^{\text{id}}(\omega, \omega_i)$ with the hat again indicating that only the dispersive terms $\hat{\gamma}_\nu^{cc}(\mathbf{k}, \omega_i)$ in the Raman vertices contribute to $\chi_{\nu,\nu}^{\text{id}}(\omega, \omega_i)$.

Turning now to the evaluation of $\hat{\chi}_{\nu,\nu}^{\text{id}}(\omega, \omega_i)$, we first note that the leading high-frequency contribution to $\hat{\chi}_{\nu,\nu}^{\text{id}}(\omega, \omega_i)$ consists of the two self-energy and two vertex-correction terms shown in Fig. 9(c). The summation of the most singular diagrams in powers of $(H'_1)^2/\omega$ can be performed by using the self-consistent form of the electron-hole propagator [26], as illustrated in Fig. 9(d). (For more details see Ref. [26].) This approach gives

$$\begin{aligned} \hat{\chi}_{\nu,\nu}^{\text{id}}(\omega, \omega_i) &\approx -\frac{1}{v} \sum_{\mathbf{k}\mathbf{k}'\sigma} \frac{\partial f_c(\mathbf{k})}{\partial E_c(\mathbf{k})} \frac{\langle |V_1^{cc}(\mathbf{k} - \mathbf{k}')|^2 \rangle}{\hbar\omega + \hbar\Sigma_\nu^{cc}(\mathbf{k}, \omega)} \\ &\times \hat{\gamma}_\nu^{cc}(\mathbf{k}, \omega_i) (\hat{\gamma}_\nu^{cc}(\mathbf{k}, \omega_i) - \hat{\gamma}_\nu^{cc}(\mathbf{k}', \omega_i)) \\ &\times \frac{1}{\hbar} [\mathcal{D}_0^{cc}(\mathbf{k}, \mathbf{k}', \omega) + \mathcal{D}_0^{cc}(\mathbf{k}', \mathbf{k}, \omega)], \end{aligned} \quad (27)$$

where $(1/\hbar)\mathcal{D}_0^{cc}(\mathbf{k}, \mathbf{k}', \omega)$ is a useful abbreviation for

$$\frac{1}{\hbar\omega + E_c(\mathbf{k}) - E_c(\mathbf{k}') + i\hbar\eta}.$$

Here $\langle \dots \rangle$ denotes averaging over the momentum transfer by the impurity. $\Sigma_\nu^{cc}(\mathbf{k}, \omega)$ is the channel-dependent

electron-hole self-energy,

$$\begin{aligned} \hbar\Sigma_\nu^{cc}(\mathbf{k}, \omega) &= -\sum_{\mathbf{q}'} \langle |V_1^{cc}(\mathbf{q}' - \mathbf{k})|^2 \rangle \left(1 - \frac{\hat{\gamma}_\nu^{cc}(\mathbf{q}', \omega_i)}{\hat{\gamma}_\nu^{cc}(\mathbf{k}, \omega_i)} \right) \\ &\times \frac{1}{\hbar} [\mathcal{D}_0^{cc}(\mathbf{k}, \mathbf{q}', \omega) + \mathcal{D}_0^{cc}(\mathbf{q}', \mathbf{k}, \omega)]. \end{aligned} \quad (28)$$

The result of the summation of diagrams in powers of $(H'_1)^2/\omega$ is thus

$$\begin{aligned} \hat{\chi}_{\nu,\nu}^{\text{id}}(\omega, \omega_i) &\approx \frac{1}{v} \sum_{\mathbf{k}\sigma} |\hat{\gamma}_\nu^{cc}(\mathbf{k}, \omega_i)|^2 \frac{\partial f_c(\mathbf{k})}{\partial E_c(\mathbf{k})} \frac{\Sigma_\nu^{cc}(\mathbf{k}, \omega)}{\omega} \\ &\times \left[1 + \frac{-\Sigma_\nu^{cc}(\mathbf{k}, \omega)}{\omega} + \left(\frac{-\Sigma_\nu^{cc}(\mathbf{k}, \omega)}{\omega} \right)^2 + \dots \right] \\ &= -\frac{1}{v} \sum_{\mathbf{k}\sigma} |\hat{\gamma}_\nu^{cc}(\mathbf{k}, \omega_i)|^2 \frac{\partial f_c(\mathbf{k})}{\partial E_c(\mathbf{k})} \frac{-\Sigma_\nu^{cc}(\mathbf{k}, \omega)}{\omega + \Sigma_\nu^{cc}(\mathbf{k}, \omega)}. \end{aligned} \quad (29)$$

This result has the correct limit for small $\hbar\omega$ in comparison with typical damping energies.

It is important to realize here that the expression (29) is obtained under an assumption that is valid for the impurity scattering processes, namely that the real part of $\Sigma_\nu^{cc}(\mathbf{k}, \omega)$ is negligibly small. In this case, we can write $\Sigma_\nu^{cc}(\mathbf{k}, \omega) \approx i\text{Im}\{\Sigma_\nu^{cc}(\mathbf{k}, \omega)\} \approx i\Gamma_\nu^{c,\text{id}}$. This can be easily generalized to weakly inelastic incoherent scattering by introducing $\Gamma_\nu^{c,\text{id}}(\omega)$. On the other hand, the introduction of H_{AF} , Eq. (5), leads to large coherent effects in $\text{Re}\{\Sigma_\nu^{cc}(\mathbf{k}, \omega)\}$. This requires the re-examination of the single-particle Hamiltonian $H_0 + H_{\text{AF}}$, with those coherence effects related to H_{AF} incorporated also in new effective vertices, and not only in $\text{Re}\{\Sigma_\nu^{cc}(\mathbf{k}, \omega)\}$. The description of this procedure is postponed to Sec. VI C.

The generalization to other correlation functions gives the universal expression

$$\hat{\chi}_{i,i}^{\text{id}}(\omega) = \frac{-i\Gamma_i^{c,\text{id}}}{\omega + i\Gamma_i^{c,\text{id}}} \frac{1}{v_0} \hat{n}_{i,i}^{\text{id}}(\mu), \quad (30)$$

for $\Sigma_i^{cc}(\mathbf{k}, \omega) \approx i\Gamma_i^{c,\text{id}}$, $i = 1, \alpha, \nu$. Here $\hat{n}_{\nu,\nu}^{\text{id}}(\mu, \omega_i)$ is the effective channel-dependent density of states at the Fermi energy of the form

$$\hat{n}_{\nu,\nu}^{\text{id}}(\mu, \omega_i) = -\frac{1}{N} \sum_{\mathbf{k}\sigma} |\hat{\gamma}_\nu^{cc}(\mathbf{k}, \omega_i)|^2 \frac{\partial f_c(\mathbf{k})}{\partial E_c(\mathbf{k})}, \quad (31)$$

and $\hat{n}_{1,1}^{\text{id}}(\mu)$ and $\hat{n}_{\alpha,\alpha}^{\text{id}}(\mu)$ are obtained by replacing $|\hat{\gamma}_\nu^{cc}(\mathbf{k}, \omega_i)|^2$ in Eq. (31) with $(\hat{q}^{cc}(\mathbf{k}, \mathbf{k}))^2 = 0$ and $(\hat{j}_\alpha^{cc}(\mathbf{k}))^2 = (j_\alpha^{cc}(\mathbf{k}))^2$, respectively. Also, we define the related effective densities $n_{i,j}^{\text{id}}(\mu, \omega_i)$ and $\bar{n}_{i,j}^{\text{id}}(\mu, \omega_i)$ using the total vertices and the constant part of vertices instead of $|\hat{\gamma}_\nu^{cc}(\mathbf{k}, \omega_i)|^2$ in Eq. (31). Evidently, $\Gamma_1^{c,\text{id}} = 0$ and $\hat{\chi}_{1,1}^{\text{id}}(\omega) = 0$, as required by the continuity equation. Also, $n_{1,1}^{\text{d}}(\mu) \equiv \hat{n}_{\alpha,\alpha}^{\text{id}}(\mu)$ and $\Gamma_1^{c,\text{d}} \equiv \Gamma_\alpha^{c,\text{id}}$, due to the gauge invariance of the optical conductivity [26].

Let us finally mention the Coulomb screening problem. The effects of the Coulomb forces on the indirect processes are described by the Hopfield series of diagrams shown in Fig. 6(b), which is an analog of the Hopfield series studied in the context of the optical conductivity [26, 39]. This series is free of the q^{-2} singularity and, for a sufficiently large relaxation rate $\Gamma_\nu^{c,\text{id}}$ (with the critical relaxation rate $\Gamma_{\nu,0}^{c,\text{id}}$ defined precisely in the following subsection), does not affect the spectra in a critical manner. Therefore, these corrections [starting with the second term in Fig. 6(b)] are neglected in the present analysis, i.e. we take $\tilde{\chi}_{\nu,\nu}^{\text{id}}(\omega, \omega_i) \approx \hat{\chi}_{\nu,\nu}^{\text{id}}(\omega, \omega_i)$.

B. Direct vs indirect contributions

When the direct and indirect processes are combined, we obtain the total Raman correlation function in the form

$$\tilde{\chi}_{\nu,\nu}^{\text{total}}(\mathbf{q}, \omega, \omega_i) \approx \tilde{\chi}_{\nu,\nu}^{\text{d}}(\mathbf{q}, \omega, \omega_i) + \hat{\chi}_{\nu,\nu}^{\text{id}}(\omega, \omega_i), \quad (32)$$

where

$$\begin{aligned} \tilde{\chi}_{\nu,\nu}^{\text{d}}(\mathbf{q}, \omega, \omega_i) &= \hat{\chi}_{\nu,\nu}^{\text{d}}(\mathbf{q}, \omega, \omega_i) + \bar{\gamma}_{\nu,\nu}^{\text{d}}(\mathbf{q}, \omega, \omega_i) \\ &+ \bar{\chi}_{\nu,1}^{\text{d}}(\mathbf{q}, \omega, \omega_i) \frac{4\pi e^2}{q^2 \varepsilon(\mathbf{q}, \omega)} \bar{\chi}_{1,\nu}^{\text{d}}(\mathbf{q}, \omega, \omega_i), \end{aligned} \quad (33)$$

using again the separation of vertices $\gamma_\nu^{cc}(\mathbf{k}, \omega_i) = \bar{\gamma}_\nu^{cc}(\omega_i) + \hat{\gamma}_\nu^{cc}(\mathbf{k}, \omega_i)$ and the corresponding separation of $\chi_{i,j}^{\text{d}}(\mathbf{q}, \omega, \omega_i)$. There is a well-defined exclusion rule here. The constant terms in the vertices participate in the direct processes and are screened by the long-range Coulomb forces. On the contrary, only the dispersive terms participate in the indirect processes. They are independent of the wave vector \mathbf{q} and are thus nearly unaffected by the long-range screening. The intensity of the former processes is proportional to small q^2 and the intensity of the latter process is proportional to the channel-dependent relaxation rates $\Gamma_\nu^{c,\text{id}}$.

To find out which of these two processes dominate the correlation functions of the high- T_c cuprates, we now compare the imaginary parts of the expressions (25) and (30). For $n_{\nu,\nu}^{\text{d}}(\mu, \omega_i) \approx \hat{n}_{\nu,\nu}^{\text{id}}(\mu, \omega_i)$ and $\Gamma_\nu^{c,\text{id}} \approx \Gamma_\nu^{c,\text{id}}$, we obtain the condition $\hbar\omega \approx aqt_{\text{pd}}$. Furthermore, $-\text{Im}\{\chi_{\nu,\nu}^{\text{id}}(\omega, \omega_i)\}$ is characterized by a maximum at $\omega = \Gamma_\nu^{c,\text{id}}$, and the critical damping energy is given roughly by $\hbar\Gamma_{\nu,0}^{c,\text{id}} \approx aqt_{\text{pd}}$, with $aq \approx 10^{-3}$ typically. For the 3D systems and $t_{\text{pd}} = 1$ eV, the result is $\Gamma_{\nu,0}^{c,\text{id}}/(2\pi c) \approx 10 \text{ cm}^{-1}$. For the usual experimental geometry in the high- T_c cuprates [$q_{\alpha'} = q_z$ and $n_{\nu,\nu}^{\text{d}}(\mu, \omega_i) \approx (t_{\perp}/t_{\text{pd}})^2 \hat{n}_{\nu,\nu}^{\text{id}}(\mu, \omega_i)$], on the other hand, the critical relaxation rate is $\Gamma_{\nu,0}^{c,\text{id}}/(2\pi c) \approx aqt_{\perp}$, i.e. well below 10 cm^{-1} . Based on this estimates, for frequencies of the outmost experimental interest, $\omega/(2\pi c) > 50 \text{ cm}^{-1}$, the direct processes can be omitted and we continue the analysis with the approximate expression

$$\tilde{\chi}_{\nu,\nu}^{\text{total}}(\mathbf{q}, \omega, \omega_i) \approx \hat{\chi}_{\nu,\nu}^{\text{id}}(\omega, \omega_i). \quad (34)$$

The measured Raman spectra $-\text{Im}\{\tilde{\chi}_{\nu,\nu}^{\text{total}}(\omega, \omega_i)\}$ are thus proportional to $-\text{Im}\{\hat{\chi}_{\nu,\nu}^{\text{id}}(\omega, \omega_i)\}$ of Eq. (30).

For comparison with experimental and previous theoretical results, it is useful to rewrite the effective densities $\hat{n}_{\nu,\nu}^{\text{id}}(\mu, \omega_i)$ in terms of the related densities $n_{i,j}^{\text{id}}(\mu, \omega_i)$, which involve the total Raman vertices. For this purpose, we notice that the constant terms $\bar{\gamma}_\nu^{cc}(\omega_i)$, defined by $n_{\nu,1}^{\text{d}}(\mu, \omega_i) = \bar{\gamma}_\nu^{cc}(\omega_i) n_{1,1}^{\text{d}}(\mu)$, can be formally expressed in terms of the effective density of states $n_{i,j}^{\text{id}}(\mu, \omega_i)$ in the following way

$$\bar{\gamma}_\nu^{cc}(\omega_i) \approx \frac{n_{\nu,1}^{\text{id}}(\mu, \omega_i)}{n_{1,1}^{\text{id}}(\mu)}. \quad (35)$$

This finally leads to

$$\begin{aligned} \hat{n}_{A_{1g}}^{\text{id}}(\mu, \omega_i) &= \frac{n_{A_{1g}}^{\text{id}}(\mu, \omega_i) n_{1,1}^{\text{id}}(\mu) - (n_{A_{1g},1}^{\text{id}}(\mu, \omega_i))^2}{n_{1,1}^{\text{id}}(\mu)}, \\ \hat{n}_\nu^{\text{id}}(\mu, \omega_i) &= n_\nu^{\text{id}}(\mu, \omega_i), \quad \nu = B_{1g}, B_{2g} \end{aligned} \quad (36)$$

[using the abbreviation $\hat{n}_\nu^{\text{id}}(\mu, \omega_i) \equiv \hat{n}_{\nu,\nu}^{\text{id}}(\mu, \omega_i)$].

C. Comparison with the usual field-theory approach

For a general reference it is interesting to notice that $\tilde{\chi}_{\nu,\nu}^{\text{d}}(\mathbf{q}, \omega, \omega_i)$ of Eq. (33) can be rewritten as

$$\begin{aligned} \tilde{\chi}_{\nu,\nu}^{\text{d}}(\mathbf{q}, \omega) &= \frac{\chi_{\nu,\nu}^{\text{d}}(\mathbf{q}, \omega) \chi_{1,1}(\mathbf{q}, \omega) - \chi_{\nu,1}^{\text{d}}(\mathbf{q}, \omega) \chi_{1,\nu}^{\text{d}}(\mathbf{q}, \omega)}{\chi_{1,1}(\mathbf{q}, \omega)} \\ &+ \frac{\chi_{\nu,1}^{\text{d}}(\mathbf{q}, \omega) \chi_{1,\nu}^{\text{d}}(\mathbf{q}, \omega)}{\chi_{1,1}(\mathbf{q}, \omega) \varepsilon(\mathbf{q}, \omega)}, \end{aligned} \quad (37)$$

in the simplified notation [ω_i is omitted and it is noted that $\chi_{1,1}^{\text{d}}(\mathbf{q}, \omega) = \chi_{1,1}(\mathbf{q}, \omega)$]. This relation is the starting point of the recent field-theory approaches (FTA) of the electronic Raman scattering [18, 22, 24, 30], and is the source of controversies regarding the role of the long-range screening appearing only in the Raman scattering in the A_{1g} channel, since $\chi_{\nu,1}^{\text{d}}(\mathbf{q}, \omega, \omega_i) = 0$ for $\nu = B_{1g}, B_{2g}$. The second A_{1g} term in Eq. (37) is usually taken to be screened out by the static screening, and the remaining expression has a structure at first sight similar to our expressions (36). Both expressions show that the A_{1g} total Raman spectrum is reduced with respect the bare spectrum [$\chi_{A_{1g},1}^{\text{d}}(\mathbf{q}, \omega, \omega_i) \neq 0$]. But, as shown above, such a FTA result is obviously incorrect, for at least two reasons: (i) The screening of the direct processes is dynamic, and accompanied by the plasmon contribution, which should be seen, if really present. (ii) All the direct contributions are proportional to small q^2 , and are, therefore, negligible when compared to the contribution of the indirect processes, Eq. (30), which do not involve the Coulomb screening at all, Eq. (34).

In the FTA, it is usually attempted to circumvent [17, 38] these difficulties by using the modified Feynman

rules in which the momentum relaxation in Eq. (24) is replaced by the energy relaxation, i.e. $f_c(\mathbf{k} + \mathbf{q}) - f_c(\mathbf{k}) \rightarrow f(E_c(\mathbf{k}) + \hbar\omega) - f(E_c(\mathbf{k}))$ for the intraband contributions. In this way, one obtains the famous field-theory expression [18, 21, 22, 30] for the screened Raman correlation function $\tilde{\chi}_{\nu,\nu}^{\text{FTA}}(\omega)$ in which the $\chi_{i,j}^{\text{id}}(\mathbf{q}, \omega)$ in Eq. (37) are replaced by

$$\begin{aligned}\chi_{i,j}^{\text{FTA}}(\omega) &= \chi_{i,j}^{\text{id}}(\omega) - \chi_{i,j}^{\text{id}}(0) \\ &= \frac{\omega}{\omega + i\Gamma_{i,j}^{\text{c,id}}} \frac{1}{v_0} n_{i,j}^{\text{id}}(\mu),\end{aligned}\quad (38)$$

and the second A_{1g} term in Eq. (37) is removed upon assuming the static screening $\varepsilon(\mathbf{q}, 0) \gg 1$. Since $\hat{\chi}_{\nu,\nu}^{\text{id}}(0)$ is real, the functions $\chi_{i,j}^{\text{FTA}}(\omega)$ and $\chi_{i,j}^{\text{id}}(\omega)$ have the same imaginary part (important to the Raman spectra). The form of the resulting $\text{Im}\{\tilde{\chi}_{\nu,\nu}^{\text{FTA}}(\omega)\}$ is thus similar to the imaginary part of our expression (34) [combined with (30), (35) and (36)].

It should, however, be noticed that the use of the static dielectric function $\varepsilon(\mathbf{q}, 0)$, either in the straightforward [22] or in the improved [30] FTA, is in contradiction with the use of $\chi_{1,1}^{\text{FTA}}(\omega)$ independent of \mathbf{q} . This contradiction is resolved by Eq. (34), which shows that the Raman response is dominated by the indirect processes, for which the long-range singularity q^{-2} in the A_{1g} channel is removed by incoherent scattering, and thus the Coulomb screening, instead of being all-important is unimportant. Eqs. (36) and (30), although widely used, are thus derived here for the first time in a consistent way.

V. INTRABAND RAMAN SPECTRAL FUNCTIONS

In order to illustrate the importance of the enhancement of the electronic Raman spectra by the interband resonance, we shall consider now the bare correlation functions $\chi_{\nu,\nu}^{\text{id}}(\omega, \omega_i)$, $\nu = A_{1g}, B_{1g}, B_{2g}$, in the Drude regime of the $H_{\text{AF}} = 0$ case, using (i) the static-Raman-vertex approximation, $\gamma_{\nu}^{\text{cc}}(\mathbf{k}, \omega_i, \omega_s) \approx \gamma_{\nu}^{\text{cc}}(\mathbf{k})$, usual in most of the current literature [17, 18, 19, 20, 21, 22, 27], and (ii) the elastic-Raman-vertex approximation [30, 46]. Also, the reduced correlation function $\hat{\chi}_{A_{1g}, A_{1g}}^{\text{id}}(\omega, \omega_i)$ will be compared to $\chi_{A_{1g}, A_{1g}}^{\text{id}}(\omega, \omega_i)$ to estimate the reduction effects present in Eq. (36). Since, in the numerical calculations discussed below, the 3D nature of the problem appears only in the relaxation rates, which are assumed to be independent of the wave vector and frequency, we set $t_{\perp} \approx 0$ and replace the 3D integrations in the correlation functions by 2D integrations.

A. Intraband (Drude) Raman scattering

For $\Sigma_{\nu}^{\text{cc}}(\mathbf{k}, \omega) \approx i\Gamma_{\nu}^{\text{c,id}}$, the spectral functions related to the Drude part of electronic Raman spectra are given by

$$-\text{Im}\{\hat{\chi}_{\nu,\nu}^{\text{id}}(\omega, \omega_i)\} \approx \frac{\omega \Gamma_{\nu}^{\text{c,id}}}{\omega^2 + (\Gamma_{\nu}^{\text{c,id}})^2} \frac{1}{v_0} \hat{n}_{\nu}^{\text{id}}(\mu, \omega_i). \quad (39)$$

For $\Gamma_{\nu}^{\text{c,id}} \approx \Gamma^{\text{c,id}}$, the three Raman channels are still distinguished by the effective Raman density of states $\hat{n}_{\nu}^{\text{id}}(\mu, \omega_i)$.

Furthermore, the comparison with the related intraband conductivity $\sigma_{\alpha\alpha}^c(\omega)$

$$\text{Re}\{\sigma_{\alpha\alpha}^c(\omega)\} = \frac{\Gamma_{\alpha}^{\text{c,id}}}{\omega^2 + (\Gamma_{\alpha}^{\text{c,id}})^2} \left(\frac{eat_{\text{pd}}}{\hbar} \right)^2 \frac{1}{v_0} n_{\alpha}^{\text{id}}(\mu), \quad (40)$$

with $(eat_{\text{pd}}/\hbar)^2 n_{\alpha}^{\text{id}}(\mu)/v_0 \equiv e^2 n_{\alpha\alpha}^{\text{eff}}/m$, where $n_{\alpha\alpha}^{\text{eff}}$ is the effective number of conduction electrons per unit cell (discussed in more detail in Sec. VI A), gives an analog of the well-known relation valid in simple Drude metals,

$$-\text{Im}\{\hat{\chi}_{\nu,\nu}^{\text{id}}(\omega, \omega_i)\} \propto \omega \text{Re}\{\sigma_{\alpha\alpha}^c(\omega)\}. \quad (41)$$

[Notice that $\hat{n}_{\alpha}^{\text{id}}(\mu) \equiv n_{\alpha}^{\text{id}}(\mu)$, because the constant term in the current vertex is equal to zero, i.e. $j_{\alpha}(-\mathbf{k}) = -j_{\alpha}(\mathbf{k})$.] Here it applies to the CuO_2 plane ($\alpha = x, y$ and $\nu = A_{1g}, B_{1g}, B_{2g}$). This relation has been verified in the measured spectra of the overdoped high- T_c cuprates [2, 3, 4, 5, 6, 7], where the relaxation rates $\Gamma_{\alpha}^{\text{c,id}}$ and $\Gamma_{\nu}^{\text{c,id}}$ have been replaced by $\Gamma(\omega) \approx \Gamma(0) + \lambda\omega$.

The SRVA version of these expressions, which sets $\omega_i = 0$ in Eq. (39), was first derived by Zawadowski and Cardona [17] and then extended to the case of strong quasi-particle damping ($\lambda \neq 0$) in Ref. [19]. For the overdoped compounds, the $\lambda \neq 0$ single component intraband term is the only contribution relevant to the experimental spectra. On the other hand, in the underdoped regime, the complete model includes both the Drude contribution (39) and the contributions of the low-lying excitations across the AF (pseudo)gap [2, 3, 47, 48, 49], discussed further in Sec. VI C.

B. Static-Raman vertex approximation

We present now the bare spectra $-\text{Im}\{\chi_{\nu,\nu}^{\text{id}}(\omega, \omega_i)\}$ relevant for the Drude regime. First we discuss the validity of the SRVA [$\omega_i = 0$ in Eq. (31)]. As mentioned above, the three-band model used in the present calculation includes the site energy splitting $\Delta_{\text{pd}} = E_{\text{p}} - E_{\text{d}}$ and the first-neighbor bond-energy t_{pd} , but neglects the second-neighbor bond-energy t_{pp} [33, 34, 36]. $n_{\alpha}(\mu)$ was evaluated previously [25] for the parameters required to give a reasonable agreement with the measured spectral weight of the visible conductivity in the La_2CuO_4 -based compounds.

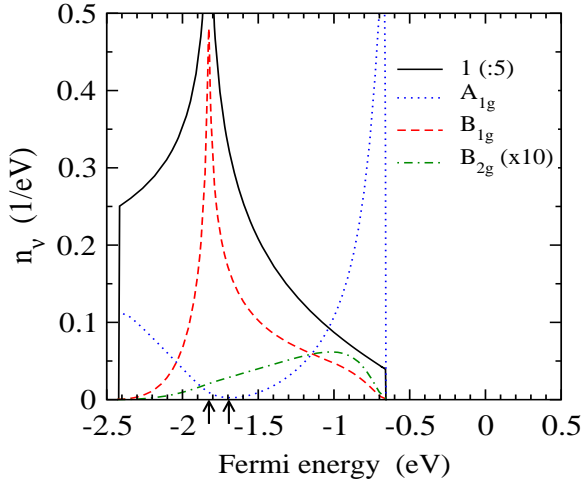


FIG. 10: The dependence of the effective density of states on the Fermi energy μ , for $\Delta_{pd} = 0.66$ eV, $t_{pd} = 0.73$ eV and $t_{pp} = 0$. The label $\nu = 1$ denotes the ordinary density of states (divided by a factor of 5), and $\nu = A_{1g}$, B_{1g} , and B_{2g} correspond to three Raman polarizations. For clarity the B_{2g} density of states is multiplied by 10. The hole picture is used, i.e. the upper band boundary corresponds to the hole doping $\delta = 1$ (measured with respect to half-filling). The doping range $0 < \delta < 0.3$, relevant to the hole doped high- T_c cuprates, is indicated by two arrows.

Using the same parameters, $n_\nu(\mu)$ is calculated now in the SRVA. Fig. 10 shows this effective density of states, representing an appropriate measure for both the maxima in the Drude part of the Raman spectra, Eq. (39), and the corresponding spectral weights. The most striking result is that in the doping range of interest, $0 < \delta < 0.3$, the ratio $n_{B_{1g}}(\mu)/n_{A_{1g}}(\mu)$ is large [typically $n_{B_{1g}}(\mu)/n_{A_{1g}}(\mu) \approx 50$]. This enhancement is related to the fact that, for $t_{pp} = 0$, the factor $[\gamma_{A_{1g}}^{cc}(\mathbf{k})]^2$ becomes negligible in comparison with $[\gamma_{B_{1g}}^{cc}(\mathbf{k})]^2$ for the Fermi energy close to the van Hove energy. This prediction of SRVA is however physically unacceptable, since the measured $n_{B_{1g}}(\mu)/n_{A_{1g}}(\mu) \approx 1$ [5, 6, 7].

Using the definition of the constant terms $\bar{\gamma}_\nu^{cc}(\omega_i)$, $n_{\nu,1}^d(\mu, \omega_i) = \bar{\gamma}_\nu^{cc}(\omega_i) n_{1,1}^d(\mu)$, we can write

$$\hat{n}_\nu^{\text{id}}(\mu) = n_\nu^{\text{id}}(\mu) - \left(\frac{n_{\nu,1}^d(\mu)}{n_{1,1}^d(\mu)} \right)^2 n_{1,1}^d(\mu) \quad (42)$$

in the simplified notation (ω_i is omitted). This expression [and its approximate version (36) as well] reveals the existence of two qualitatively different regimes: (i) For the nearly half-filled conduction band, i.e. for the Fermi energy close to the van Hove energy, the second term is negligible [$n_{\nu,1}^d(\mu)$ crosses zero at $\delta \approx 0.3$, and $n_{1,1}^d(\mu)$ is singular for $\mu \approx \varepsilon_{\text{vH}}$]. For $\mu \approx \varepsilon_{\text{vH}}$, the constant term in the A_{1g} Raman vertex is negligibly small. (ii) On the contrary, for the doping well away from half-filling, the dispersive terms in the vertices are negligible, leading to the strong reduction effects in Eq. (42) with

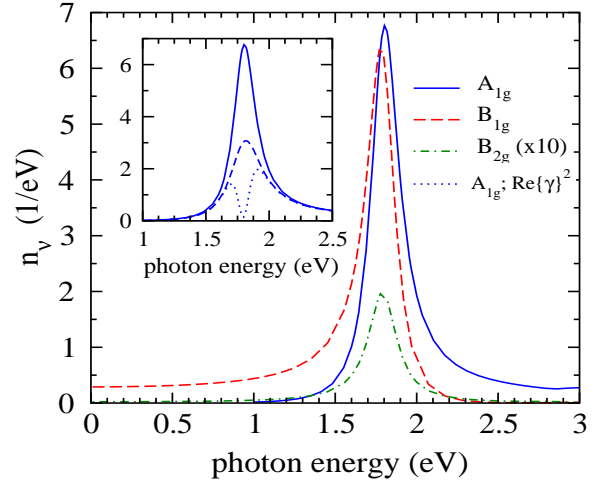


FIG. 11: Inset: The resonant enhancement of the A_{1g} density of states $n_{A_{1g}}$ for $\delta = 0.1$ ($\mu = -1.793$ eV in Fig. 10), and $\hbar\Gamma^{\text{inter}} = 0.1$ eV (solid and dotted line) and 0.15 eV (dashed line). The dotted (solid, dashed) line represents the contributions of the real (real and imaginary) part(s) in $\gamma_\nu^{cc}(\mathbf{k}, \omega_i)$ to $n_{A_{1g}}$. Main figure: The total bare effective density of states for all three Raman channels for $\hbar\Gamma^{\text{inter}} = 0.1$ eV. The B_{2g} spectrum is again multiplied by 10.

$$\hat{n}_{A_{1g}}^{\text{id}}(\mu) \ll n_{A_{1g}}^{\text{id}}(\mu).$$

To simplify the discussion of the resonant effects and the effects of the AF correlations, in the rest of the article we consider the effective density of states $\hat{n}_\nu^{\text{id}}(\mu) \approx n_\nu^{\text{id}}(\mu)$. For $0 < \delta < 0.3$, the corrections are of the order of few percent, i.e. they are comparable to the effects of the orthorhombic distortion on $\tilde{\chi}_{\nu,\nu}^{\text{total}}(\mathbf{q}, \omega, \omega_i)$ which have been already neglected here.

C. Elastic-Raman vertex approximation

We calculate therefore the effective density of states $n_\nu(\mu, \omega_i)$ in the ERVA, i.e. retaining ω_i in Eq. (31), for the hole doping $\delta = 0.1$ and the damping energies $\hbar\Gamma^{\text{inter}} = 0.1$ and 0.15 eV. In Fig. 11 we show the results for the model parameters used above ($\Delta_{pd} = 0.66$ eV and $t_{pd} = 0.73$ eV). For $\hbar\omega_i \approx 0$, the large $n_{B_{1g}}(\mu, \omega_i)$ intraband term, associated with van Hove singularities, is large with respect to the interband $n_{A_{1g}}(\mu, \omega_i)$ term. For $\hbar\omega_i$ around $E_N(\mathbf{k}) - \mu \approx 1.8$ eV (N for the non-bonding band), the resonant (interband) contribution to $n_{A_{1g}}(\mu, \omega_i)$ is nearly equal to the sum of the static (intraband) and resonant (interband) terms in $n_{B_{1g}}(\mu, \omega_i)$. In the maximum, the comparable interband contributions dominate. This energy range corresponds to $E_N(\mathbf{k}) - \mu < \hbar\omega_i < (E_N(\mathbf{k}) - E_c(\mathbf{k}))_{\text{max}}$, because for $t_{pp} = 0$, the optical excitations between the conduction and antibonding bands are negligible [36]. For t_{pp} large enough, the latter excitations become important as well, and resonant effects are extended to the energy region $E_N(\mathbf{k}) - \mu < \hbar\omega_i < (E_P(\mathbf{k}) - E_c(\mathbf{k}))_{\text{max}}$ (i.e.

between 1.7 and 4 eV). Due to the resonant enhancement of the Raman scattering processes, we find the ratio $n_{B_{1g}}(\mu, \omega_i)/n_{A_{1g}}(\mu, \omega_i)$ consistent with the experimental observation. Notice, however, the reduction of the resonant effect with increasing damping energy $\hbar\Gamma^{\text{inter}}$ (inset of the figure).

The spectral weight of the B_{2g} channel relative to two other channels turns out to be one order of magnitude smaller than the one usually found in experiments. This reflects the fact that various processes described by other parameters of the three-band model, and in particular by the direct oxygen-oxygen hopping t_{pp} , are absent here. It should be noticed that t_{pp} opens an additional channel in the electron-photon coupling [see Eq. (A3)] involving predominantly the electronic states in the nodal $k_x = k_y$ region of the Fermi surface. As easily seen, this leads in the first place to the enhancement of the B_{2g} Raman spectra giving the contributions proportional to t_{pp} in $\gamma_{B_{2g}}^{cc}(\mathbf{k}, \omega_i)$, additional to the contributions of the indirect oxygen-oxygen hopping processes ($\propto t_{\text{pd}}^2$) shown in Figs. 10–11.

We notice finally that, if the contributions of $\text{Im}\{\gamma_{\nu}^{CC}(\mathbf{k}, \omega_i)\}$ to $n_{\nu}(\mu, \omega_i)$ are neglected, one obtains the resonant structure characterized by two peaks split approximately by the energy $2\hbar\Gamma^{\text{inter}}$, as represented in the inset of Fig. 11 by the dotted line. Similar dependence of the Raman spectra on the photon frequencies was already proposed in the multiband study of the electron-mediated photon-phonon coupling functions [46].

It should be noticed that most of the recent Raman studies are focussed only on the B_{1g} and B_{2g} channels. These two channels scan the complementary parts of the Fermi surface (the vicinity of the van Hove points in B_{1g} and the nodal region of the Brillouin zone in B_{2g}) and almost all relevant physics is present in the related spectra [7, 13, 49]. Our comparison with the experimental data, given in Sec. VI C, will be thus also limited to these two channels.

VI. EFFECTS OF THE AF ORDERING

The effective potential describing the AF correlation effects is peaked at $\mathbf{Q}_{\text{AF}} = (\pi/a, \pi/a)$ with the \mathbf{k} dependence assumed to be of the $d_{x^2-y^2}$ and anisotropic- s symmetry: $\Delta(\mathbf{k}) = 0.5\Delta_0(\cos \mathbf{k} \cdot \mathbf{a}_1 - \cos \mathbf{k} \cdot \mathbf{a}_2)$ and $\Delta(\mathbf{k}) = \Delta_0\sqrt{0.5 + 0.125(\cos \mathbf{k} \cdot \mathbf{a}_1 - \cos \mathbf{k} \cdot \mathbf{a}_2)^2}$, respectively. This potential dominantly affects the states close to the van Hove points, leads to the dimerization of the bands, and is accompanied by the low-lying interband processes characterized by a threshold energy proportional to the magnitude Δ_0 . Two subbands of the conduction band will be denoted by the indices $L = C$ (upper band) and $L = \underline{C}$ (lower band). For the half-filled conduction band of the $t_{\text{pp}} = 0$ model, \mathbf{Q}_{AF} leads to the ideal nesting of the Fermi surface and, correspondingly, the relevance of this perturbation grows with de-

creasing hole doping. For finite t_{pp} , the interplay between t_{pp} and $\Delta(\mathbf{k})$ is of the central importance, and is probably responsible for the anomalies regarding the development of both the Fermi surface shape [37] and the optical conductivity with doping. Namely, for t_{pp} large enough, even small changes in the hole doping could produce dramatic changes in the electrodynamic features of the electron system (this might be analogous to the situation found in the quasi-one-dimensional Bechgaard salts [51]). ARPES measurements in the $\text{YBa}_2\text{C}_3\text{O}_{7-x}$ and Bi-based cuprates [52, 53] are indicative of such a regime. In this respect the measurements in the La_2CuO_4 based compounds, where t_{pp} can be neglected, are in the focus of the present discussion.

A more rigorous treatment should introduce the AF correlations through the time-dependent pseudogap $\Delta(\mathbf{k}, t)$ [37], rather than through the dimerization potential $\Delta(\mathbf{k})$ added to H_0 . However, for our qualitative purposes, the present treatment of the AF correlation effects is sufficient. To further justify this approximation we shall compare now the theoretical predictions for the DC conductivity and the Hall number with the measurements in the underdoped La_2CuO_4 -based compounds. In the overdoped compounds, on the other hand, the models with the dynamical treatment of AF correlations are necessary [19].

A. Hall coefficient

In the three-band model with the magnetic field normal to the conduction plane, the room-temperature Hall coefficient is of the form $R_{\text{H}} \approx 1/(ecn_{\text{H}})$, where n_{H} is the effective Hall number given by $n_{\text{H}} = n_{xx}^{\text{eff}}n_{yy}^{\text{eff}}/n_{xy}^{\text{eff}}$. The diagonal and off-diagonal effective numbers of charge carriers read as [25, 54, 57]

$$n_{\alpha\alpha}^{\text{eff}} = -\frac{m}{e^2} \frac{1}{v} \sum_{\mathbf{k}^*\sigma} [J_{\alpha}^{CC}(\mathbf{k})]^2 \frac{\partial f_C(\mathbf{k})}{\partial E_C(\mathbf{k})}, \quad (43)$$

$$n_{xy}^{\text{eff}} = \frac{m}{e^2} \frac{1}{v} \sum_{\mathbf{k}^*\sigma} \frac{\partial f_C(\mathbf{k})}{\partial E_C(\mathbf{k})} J_x^{CC}(\mathbf{k}) [\gamma_{yy}^{CC}(\mathbf{k}) J_x^{CC}(\mathbf{k}) - \gamma_{xy}^{CC}(\mathbf{k}) J_y^{CC}(\mathbf{k})] \quad (44)$$

($\alpha = x$ or y). The structure of the intraband current vertices, $J_{\alpha}^{CC}(\mathbf{k})$ [$J_{\alpha}^{cc}(\mathbf{k})$], and the static Raman vertices, $\gamma_{\alpha\beta}^{CC}(\mathbf{k})$ [$\gamma_{\alpha\beta}^{cc}(\mathbf{k})$], for the $\Delta_0 \neq 0$ ($\Delta_0 = 0$) case is determined in Appendix B (A). For $\Delta_0 \neq 0$ ($\Delta_0 = 0$), $\mathbf{k}^*(\mathbf{k})$ refers to the new (old) Brillouin zone. The DC conductivity can be scaled by the diagonal effective numbers, as well, according to the relations (40) and (43), $\sigma_{\alpha\alpha}^{\text{DC}} = e^2 n_{\alpha\alpha}^{\text{eff}} / (m\Gamma_{\alpha}^{\text{c,id}})$.

The effective numbers (43) and (44) are extremely sensitive to the correlation effects. In order to illustrate this dependence, the numbers n_{xx}^{eff} and n_{H} are calculated with and without the potential $\Delta(\mathbf{k})$ of the $d_{x^2-y^2}$ symmetry and are compared to the experimental observations in $\text{La}_{2-x}\text{Sr}_x\text{CuO}_4$ [2, 32] showing that (i) the change of the

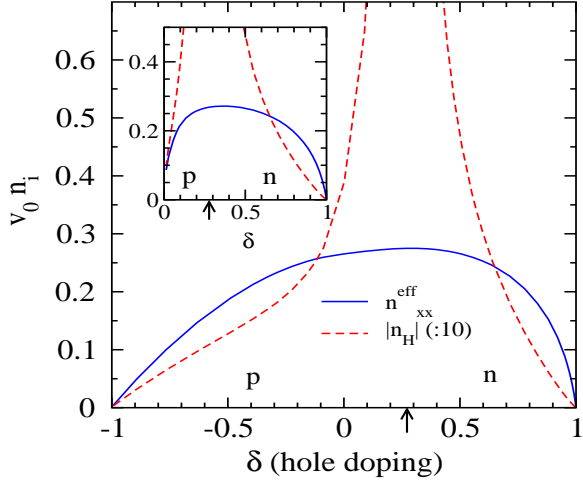


FIG. 12: Main frame: Effective numbers n_{xx}^{eff} and $|n_H|$ (representing also the DC conductivity and the inverse Hall coefficient, scaled by $e^2/(mv_0\Gamma_x^{c,id})$ and ec/v_0 , respectively) as a function of the doping level for $\Delta_0 = 0$. Inset: The effect of the AF correlations on n_{xx}^{eff} and $|n_H|$ for the $d_{x^2-y^2}$ symmetry perturbation $\Delta(\mathbf{k})$ with $\Delta_0 = 50$ meV, in the hole-doped region. The critical doping δ_0 , where $n_{xy}^{eff} = 0$, is labeled by arrows. n and p denote, respectively, the region of electron-like ($n_H, n_{xy}^{eff} < 0$) and hole-like ($n_H, n_{xy}^{eff} > 0$) behavior of the charge carriers.

sign of n_H occurs nearly at $\delta_0 \approx 0.25$; (ii) $n_H \propto \delta$ in the underdoped compounds; and (iii) $n_{\alpha\alpha}^{eff} \propto \delta$ for $\delta \rightarrow 0$. The results are given in Fig. 12 for $\Delta_0 = 0$ and 50 meV. The main figure illustrates the well-known fact that for a pair of bonding and antibonding bands the critical doping δ_0 , which separates the electron-like doping region(s) from the hole-like one(s), is shifted for finite t_{pd}/Δ_{pd} ($t_{pp} = 0$) from $\delta = 0$ in the positive (negative) direction for the lower (upper) band, breaking in this way a simple electron-hole symmetry in each of these two bands. For the wide conduction band, characterized by $\Delta_{pd} = 0.66$ eV and $t_{pd} = 0.73$ eV, this results in $\delta_0 \approx 0.27$, in agreement with the observation (i). The measured linear δ -dependences of n_{xx}^{eff} (iii) and n_H (ii) can be related to the mid-infrared (MIR) gap structure, as seen from the inset of Fig. 12. It should also be noticed that, for Δ_0 not too large, the position of δ_0 is only slightly dependent on Δ_0 . More importantly, due to the doubled number of zeros of $\partial^2 E_C(\mathbf{k})/\partial k_\alpha \partial k_\beta$ (which appear above and below the original van Hove energy ε_{vH}), the effective number n_{xy}^{eff} has two zeros, resulting in an additional critical doping within the electron-doped range. In crude terms, this restores the electron-hole symmetry of the phase diagram of the high- T_c cuprates, which is seen in the Hall coefficient measurements [2, 32].

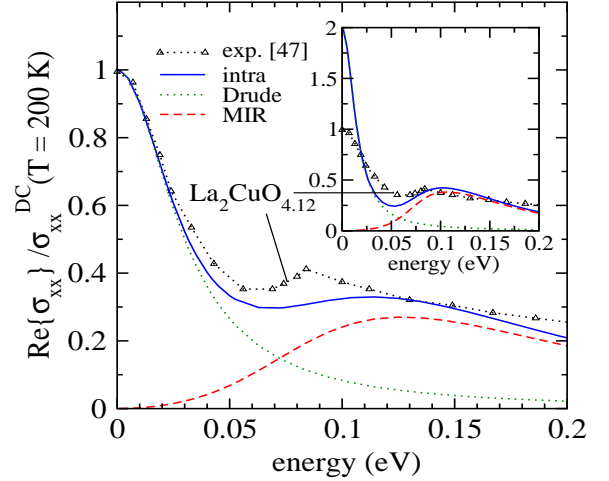


FIG. 13: The optical conductivity (45) for the anisotropic-s potential $\Delta(\mathbf{k})$ with $\Delta_0 = 45$ meV, $\Delta_{pd} = 0.66$ eV, $t_{pd} = 0.73$ eV, $\delta = 0.1$, $\zeta_1 = 0.18$ and $\zeta_2 = 0.4$. Main figure: $\hbar\Gamma_\alpha^{c,id} = 30$ meV and $\hbar\Gamma_\alpha^{MIR} = 50$ meV (suitable to $T = 200$ K spectra in the La_2CuO_4 based compounds). Inset: $\hbar\Gamma_\alpha^{c,id} = 15$ meV and $\hbar\Gamma_\alpha^{MIR} = 25$ meV ($T \approx 100$ K). The data measured in $\text{La}_2\text{CuO}_4.12$ at $T = 200$ K [47] connected by the dotted line are given for comparison.

B. Optical conductivity

The dependence of the low-frequency conductivity on the symmetry and magnitude of the dimerization potential $\Delta(\mathbf{k})$ is analyzed in detail in Refs. [25, 26]. For the sake of completeness we enumerate here the most important results. The two-component $\Delta_0 \neq 0$ intraband conductivity reads

$$\sigma_{\alpha\alpha}^{\text{intra}}(\omega) \approx \zeta_1 \frac{i}{\omega} \frac{e^2 n_{\alpha\alpha}^{eff}}{m} \frac{\omega}{\omega + i\Gamma_\alpha^{c,id}} - \zeta_2 i\omega \alpha_{\alpha\alpha}^{\text{MIR}}(\omega), \quad (45)$$

with the effective number of conduction electrons, $n_{\alpha\alpha}^{eff}$, and the MIR polarizability, $\alpha_{\alpha\alpha}^{\text{MIR}}(\omega)$, given by

$$n_{\alpha\alpha}^{eff} = \frac{1}{v} \sum_{\mathbf{k}^* \sigma} \gamma_{\alpha\alpha}^{CC}(\mathbf{k}) [1 - f_C(\mathbf{k})], \quad (46)$$

$$\alpha_{\alpha\alpha}^{\text{MIR}}(\omega) = \frac{1}{\omega^2} \frac{1}{v} \sum_{\mathbf{k}^* \sigma} \frac{(\hbar\omega)^2 |J_\alpha^{CC}(\mathbf{k})|^2}{E_{CC}^2(\mathbf{k})} \times \frac{2E_{CC}(\mathbf{k}) [f_C(\mathbf{k}) - 1]}{(\hbar\omega + i\hbar\Gamma_\alpha^{\text{MIR}})^2 - E_{CC}^2(\mathbf{k})}. \quad (47)$$

The renormalization factors ζ_1 and ζ_2 in Eq. (45) serve here to model the effects of fluctuations of auxiliary bosons on the low-frequency optical excitations [25]. The vertex $J_\alpha^{CC}(\mathbf{k})$ and the energy difference $E_{CC}(\mathbf{k})$ are given in Appendix B.

Fig. 13 illustrates the typical low-frequency spectra measured in $\text{La}_2\text{CuO}_4.12$, compared to the model predictions. In spite of its simplicity, the model (45)–(47)

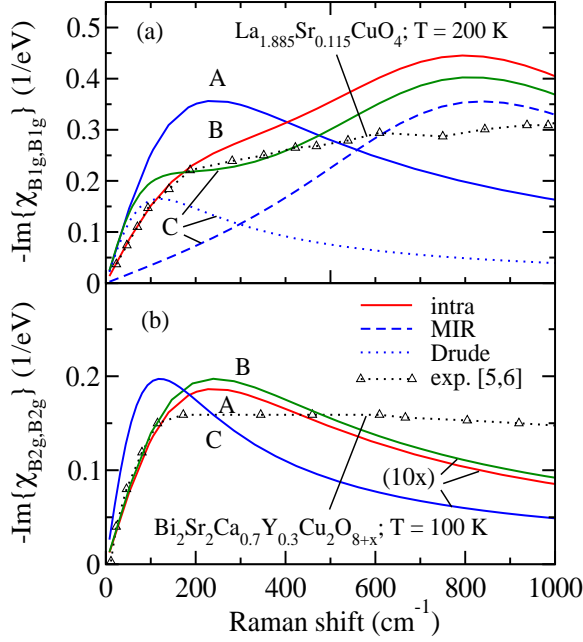


FIG. 14: The B_{1g} (a) and B_{2g} (b) electronic Raman spectra obtained by ERVA for the $d_{x^2-y^2}$ symmetry potential $\Delta(\mathbf{k})$. The parameters are $\Delta_{pd} = 0.66$ eV, $t_{pd} = 0.73$ eV, $\delta = 0.1$, $\hbar\omega_i = 2$ eV, $\hbar\Gamma_{\nu}^{\text{MIR}} = 50$ meV and $\hbar\Gamma_{\nu}^{\text{inter}} = 0.1$ eV. The curves A (B): $\Delta = 0$ (45) meV and $\hbar\Gamma_{\nu}^{c,id} = 30$ meV. The curves C: $\Delta_0 = 45$ meV and $\hbar\Gamma_{\nu}^{c,id} = 15$ meV [with the Drude (dotted line) and MIR (dashed line) contributions indicated as well]. The B_{2g} spectrum is multiplied by 10. The experimental data (connected by the dotted line and shown in arbitrary units) measured in the underdoped compounds $\text{La}_{1.885}\text{Sr}_{0.115}\text{CuO}_4$ (B_{1g} at $T = 200$ K [5]) and $\text{Bi}_2\text{Sr}_2\text{Ca}_{0.7}\text{Y}_{0.3}\text{Cu}_2\text{O}_{8+x}$ (B_{2g} at $T = 100$ K [6]) are given for comparison.

with $t_{pp} = 0$ can explain why the MIR structure in $\text{La}_2\text{CuO}_{4.12}$ is nearly independent of temperature [47]. Namely, at temperatures below the room temperature, the position of the MIR maximum $\hbar\omega_{\text{MIR}} \approx 90$ meV is well above the relaxation rate $\hbar\Gamma_{\alpha}^{\text{MIR}}$ and correspondingly $\hbar\omega_{\text{MIR}} \approx 2\Delta_0$, independent of $\hbar\Gamma_{\alpha}^{\text{MIR}}$. This situation strongly contrasts with those observed in the Bechgaard salts [51] or in $\text{Bi}_2\text{SrCuO}_6$ [48] where small Drude spectral weights (i.e. $v_0 n_{\alpha\alpha}^{\text{eff}} \ll 1$) reveal the interplay between t_{pp} (or t_b in the Bechgaard salts) and the energy scale $2\Delta_0$ [41].

C. B_{1g} and B_{2g} Raman spectra

Next, we extend the discussion of the AF effects to the electronic Raman spectra. In the hole-doped regime, the Drude-like contributions and the low-lying transitions through the AF (pseudo)gap are given by Eq. (39) and

by

$$-\text{Im}\{\chi_{\nu,\nu}^{\text{MIR}}(\omega, \omega_1)\} \approx \frac{1}{N} \sum_{\mathbf{k}^* \sigma} |\gamma_{\nu}^{CC}(\mathbf{k}, \omega_1)|^2 [f_C(\mathbf{k}) - 1] \times \text{Im} \left\{ \frac{2E_{CC}(\mathbf{k})}{(\hbar\omega + i\hbar\Gamma_{\nu}^{\text{MIR}})^2 - E_{CC}^2(\mathbf{k})} \right\}, \quad (48)$$

respectively. Neglecting the effects of $\Delta(\mathbf{k})$ on the intermediate interband processes and applying the static approximation for the low-frequency part of the Raman vertex, the elastic Raman vertices in the expressions (39) and (48) are given by

$$\begin{aligned} \gamma_{\nu}^{CC}(\mathbf{k}, \omega_i) &\approx \gamma_{\nu}^{cc}(\mathbf{k}, \omega_i) \cos^2 \frac{\varphi(\mathbf{k})}{2} \\ &+ \gamma_{\nu}^{cc}(\mathbf{k} \pm \mathbf{Q}_{\text{AF}}, \omega_i) \sin^2 \frac{\varphi(\mathbf{k})}{2}, \\ \gamma_{\nu}^{CC}(\mathbf{k}, \omega_i) &\approx \frac{1}{2} [\gamma_{\nu}^{cc}(\mathbf{k}, \omega_i) - \gamma_{\nu}^{cc}(\mathbf{k} \pm \mathbf{Q}_{\text{AF}}, \omega_i)] \sin \varphi(\mathbf{k}). \end{aligned} \quad (49)$$

$\varphi(\mathbf{k})$ is an auxiliary phase defined in Appendix B.

Again, for $\Delta_0 \ll t_{pd}, \Delta_{pd}$, the $d_{x^2-y^2}$ symmetry potential causes significant changes in the Raman spectra only for relatively small doping ($\delta < 0.15$). The most important qualitative results are illustrated in Fig. 14 for $\delta = 0.1$ and $\Delta_0 = 0, 45$ meV.

First of all, we observe that for $t_{pp} = 0$ the MIR peak in the optical conductivity is accompanied by the occurrence of a similar peak in the Raman spectra, but only in the B_{1g} channel. Second, the anomalous weakening of the Drude part of the B_{1g} spectra by one order of magnitude with respect to the B_{2g} spectra, observed in $\text{La}_{2-x}\text{Sr}_x\text{CuO}_4$ on decreasing doping below $\delta = 0.1$ [13], is a natural consequence of the (pseudo)gap features in the electron dispersion in the vicinity of the van Hove points. Namely, the van Hove singularity in the B_{1g} effective density of states (shown in Fig. 10) is strongly suppressed for $|\varepsilon_{\text{vH}} - \mu| < \Delta_0$, in contrast to the B_{2g} case where the spectra come dominantly from the nodal region of the Fermi surface, unaffected by $\Delta(\mathbf{k})$.

VII. CONCLUSION

The electronic Raman correlation functions have been calculated for the Emery three-band model, using the distinction between the direct and indirect scattering on the inhomogeneities. It is shown that there is a simple exclusion rule connecting these two scatterings and the long-range Coulomb screening. The direct processes involve the constant terms in the vertices. They are strongly affected by the long-range screening, and, in the dynamic limit, participate in the correlation functions through the contributions proportional to small q^2 . The indirect processes include only the dispersive terms in the vertices. They are nearly unaffected by the long-range forces, and

their contributions to the correlation functions are proportional to the channel-dependent relaxation rates. It is shown that, in the high- T_c cuprates, the contributions of the direct processes to the Raman correlation functions can be safely neglected. Using the elastic approximation for the Raman vertices in two [with and without the AF dimerization potential $\Delta(\mathbf{k})$] analytically solvable versions of the $t_{\text{pp}} = 0$ Emery three-band model, we show that the resonant Raman scattering processes remove a large discrepancy between the spectral weights of the A_{1g} and B_{1g} Raman channels obtained in the static approximation for the Raman vertices. The resulting spectra agree reasonably well with experimental findings. It is also shown that the anomalous MIR peak in the optical conductivity, observed in the under-doped compounds, is correlated with the corresponding structure which appears only in the B_{1g} Raman channel, as well as with the measured linear δ -dependence of the Hall number. This relation is explained here in terms of the $\Delta(\mathbf{k}) \neq 0$ AF correlations. On the other hand, the $\Delta(\mathbf{k}) = 0$ Emery model used to fit the overall band structure, a part of which is seen in the ARPES data [14], leads to different results. Particularly noteworthy in this respect are Raman selection rules. The small energy scales observed in the Raman scattering, just as in the ARPES data [37], are therefore better related to the AF correlation effects within the conduction band than to the low-energy interband transitions in the strongly correlated $\Delta(\mathbf{k}) = 0$ metallic state.

Acknowledgement

This research was supported by the Croatian Ministry of Science and Technology under Project 0119-256.

APPENDIX A: THREE-BAND VERTEX FUNCTIONS

The coupling of the vector potential $\mathbf{A}(\mathbf{r})$ to the conduction electrons of the Emery three-band model is given in the usual way [41], by replacing the hole creation (and annihilation) operators in the bare Hamiltonian H_0 by

$$\tilde{l}_{n\sigma}^\dagger = l_{n\sigma}^\dagger e^{ie/(\hbar c)(\mathbf{R}_n + \mathbf{r}_l) \cdot \mathbf{A}(\mathbf{R}_n + \mathbf{r}_l)} \quad (\text{A1})$$

(similar for $\tilde{l}_{n\sigma}$). Here \mathbf{R}_n and \mathbf{r}_l are, respectively, the Bravais lattice vector and the position in the primitive cell of the orbital labeled by the index l . The Taylor expansion in the vector potential of \tilde{H}_0 to the second order leads to

$$\tilde{H}_0 - H_0 \approx H^{\text{ext}} = \sum_{ll' \mathbf{k} \mathbf{q} \sigma} \delta H_0^{ll'}(\mathbf{k}, \mathbf{q}) l_{\mathbf{k} + \mathbf{q} \sigma}^\dagger l'_{\mathbf{k} \sigma}, \quad (\text{A2})$$

where

$$\begin{aligned} \delta H_0^{ll'}(\mathbf{k}, \mathbf{q}) \approx & -\frac{1}{c} \frac{e}{\hbar} \sum_{\alpha} \frac{\partial H_0^{ll'}(\mathbf{k})}{\partial k_{\alpha}} A_{\alpha}(\mathbf{q}) \\ & + \frac{e^2}{2mc^2} \frac{m}{\hbar^2} \sum_{\mathbf{q}' \alpha \beta} \frac{\partial^2 H_0^{ll'}(\mathbf{k})}{\partial k_{\alpha} \partial k_{\beta}} A_{\alpha}(\mathbf{q} - \mathbf{q}') A_{\beta}(\mathbf{q}'). \end{aligned} \quad (\text{A3})$$

In the Bloch representation, H^{ext} is given by the expression (9), with the vertex functions

$$\begin{aligned} J_{\alpha}^{LL'}(\mathbf{k}) &= \frac{e}{\hbar} \sum_{ll'} \frac{\partial H_0^{ll'}(\mathbf{k})}{\partial k_{\alpha}} U_{\mathbf{k}}(l, L) U_{\mathbf{k}}^*(l', L'), \\ \gamma_{\alpha \beta}^{LL'}(\mathbf{k}; 2) &= -\frac{m}{\hbar^2} \sum_{ll'} \frac{\partial^2 H_0^{ll'}(\mathbf{k})}{\partial k_{\alpha} \partial k_{\beta}} U_{\mathbf{k}}(l, L) U_{\mathbf{k}}^*(l', L') \end{aligned} \quad (\text{A4})$$

($\alpha, \beta = x, y$).

The number of channels in the electron-photon coupling is equal to the number of independent bond energies; t_{pd} and t_{pp} in the Emery three-band model for the in-plane processes. For the $t_{\text{pp}} = 0$ three-band model, one obtains the dimensionless in-plane current and bare Raman vertices ($\alpha = x$ or y) of the form [25]

$$\begin{aligned} j_{\alpha}^{cc}(\mathbf{k}) &= t_{\text{pd}} \frac{2u_{\mathbf{k}}v_{\mathbf{k}}}{t_{\mathbf{k}}} \sin \mathbf{k} \cdot \mathbf{a}_{\alpha}, \\ j_{\alpha}^{cP}(\mathbf{k}) &= t_{\text{pd}} \frac{u_{\mathbf{k}}^2 - v_{\mathbf{k}}^2}{t_{\mathbf{k}}} \sin \mathbf{k} \cdot \mathbf{a}_{\alpha}, \\ j_x^{cN}(\mathbf{k}) &= t_{\text{pd}} \frac{2u_{\mathbf{k}}}{t_{\mathbf{k}}} \sin \frac{1}{2}\mathbf{k} \cdot \mathbf{a}_2 \cos \frac{1}{2}\mathbf{k} \cdot \mathbf{a}_1, \\ j_y^{cN}(\mathbf{k}) &= -t_{\text{pd}} \frac{2u_{\mathbf{k}}}{t_{\mathbf{k}}} \sin \frac{1}{2}\mathbf{k} \cdot \mathbf{a}_1 \cos \frac{1}{2}\mathbf{k} \cdot \mathbf{a}_2, \end{aligned} \quad (\text{A5})$$

and

$$\gamma_{\alpha \beta}^{cc}(\mathbf{k}; 2) = \delta_{\alpha, \beta} \frac{m}{m_{xx}} \frac{\Delta_{\text{pd}} u_{\mathbf{k}} v_{\mathbf{k}}}{t_{\mathbf{k}}} \sin^2 \frac{1}{2}\mathbf{k} \cdot \mathbf{a}_{\alpha}, \quad (\text{A6})$$

respectively, with

$$J_{\alpha}^{LL'}(\mathbf{k}) = \frac{e a t_{\text{pd}}}{\hbar} j_{\alpha}^{LL'}(\mathbf{k}). \quad (\text{A7})$$

$u_{\mathbf{k}}$, $v_{\mathbf{k}}$, and $t_{\mathbf{k}}$ are the auxiliary functions defined in Ref. [36], and $m_{xx} = \hbar^2 \Delta_{\text{pd}} / (2a^2 t_{\text{pd}}^2)$ is the in-plane mass scale ($|\mathbf{a}_1| = |\mathbf{a}_2| = a$).

APPENDIX B: VERTEX FUNCTIONS WITH AF

The dimerization of the conduction band $E_c(\mathbf{k})$ caused by H_{AF} is solved elsewhere [25]. The vertex functions important for the present analysis can be shown in terms of the auxiliary phase defined by

$$\tan \varphi(\mathbf{k}) = \frac{2\Delta(\mathbf{k})}{E_c(\mathbf{k}) - E_c(\mathbf{k} \pm \mathbf{Q}_{\text{AF}})}. \quad (\text{B1})$$

The static Raman vertex and the current vertices relevant to both the effective numbers (43)–(44) and the optical conductivity (45) are given, respectively, by

$$\begin{aligned} \gamma_{\alpha\alpha}^{CC}(\mathbf{k}) &= \gamma_{\alpha\alpha}^{cc}(\mathbf{k}) \cos^2 \frac{\varphi(\mathbf{k})}{2} + \gamma_{\alpha\alpha}^{cc}(\mathbf{k} \pm \mathbf{Q}_{\text{AF}}) \sin^2 \frac{\varphi(\mathbf{k})}{2} \\ &\quad - \frac{m}{e^2} \frac{2|J_{\alpha}^{CC}(\mathbf{k})|^2}{E_{C\underline{C}}(\mathbf{k})}, \end{aligned} \quad (\text{B2})$$

and

$$\begin{aligned} J_{\alpha}^{CC}(\mathbf{k}) &= J_{\alpha}^{cc}(\mathbf{k}) \cos^2 \frac{\varphi(\mathbf{k})}{2} + J_{\alpha}^{cc}(\mathbf{k} \pm \mathbf{Q}_{\text{AF}}) \sin^2 \frac{\varphi(\mathbf{k})}{2}, \\ J_{\alpha}^{C\underline{C}}(\mathbf{k}) &= \frac{1}{2}[J_{\alpha}^{cc}(\mathbf{k}) - J_{\alpha}^{cc}(\mathbf{k} \pm \mathbf{Q}_{\text{AF}})] \sin \varphi(\mathbf{k}). \end{aligned} \quad (\text{B3})$$

Here $E_{C\underline{C}}(\mathbf{k}) = E_C(\mathbf{k}) - E_{\underline{C}}(\mathbf{k})$ and

$$\begin{aligned} E_{C,\underline{C}}(\mathbf{k}) &= \frac{1}{2}[E_c(\mathbf{k}) + E_c(\mathbf{k} \pm \mathbf{Q}_{\text{AF}})] \\ &\quad \pm \sqrt{\frac{1}{4}[E_c(\mathbf{k}) - E_c(\mathbf{k} \pm \mathbf{Q}_{\text{AF}})]^2 + \Delta^2(\mathbf{k})}. \end{aligned} \quad (\text{B4})$$

Similarly, the approximate expressions for the total Raman vertices are given by the expressions (49).

APPENDIX C: LONGITUDINAL RESPONSE THEORY IN THE MULTIBAND MODELS

We consider the Hamiltonian (1) with $H'_2 = 0$ and H^{ext} given by Eq. (11). H'_1 includes only the time-independent impurity scattering processes. We introduce the retarded electron-hole propagator $\mathcal{D}^{LL'}(\mathbf{k}, \mathbf{k}_+, \mathbf{k}'_+, \mathbf{k}', t)$ defined by (hereafter $\mathbf{q} = q_{\alpha} \hat{e}_{\alpha}$)

$$\begin{aligned} \mathcal{D}^{LL'}(\mathbf{k}, \mathbf{k}_+, \mathbf{k}'_+, \mathbf{k}', t) &= -i\Theta(t)\langle [L_{\mathbf{k}\sigma}^{\dagger}(t)L_{\mathbf{k}+\mathbf{q}\sigma}^{\dagger}(t), L_{\mathbf{k}'+\mathbf{q}\sigma}^{\dagger}(0)L_{\mathbf{k}'\sigma}(0)] \rangle, \end{aligned} \quad (\text{C1})$$

and the related induced density

$$\begin{aligned} \delta n^{LL'}(\mathbf{k}, \mathbf{k}_+, \omega) &\equiv \delta n^{LL'}(\mathbf{k}) \\ &= \sum_{\mathbf{k}'} \frac{1}{\hbar} \mathcal{D}^{LL'}(\mathbf{k}, \mathbf{k}_+, \mathbf{k}'_+, \mathbf{k}', \omega) q^{L'L}(\mathbf{k}'_+, \mathbf{k}') V^{\text{ext}}(\mathbf{q}, \omega). \end{aligned} \quad (\text{C2})$$

The equation of motion for $\mathcal{D}^{LL'}(\mathbf{k}, \mathbf{k}_+, \mathbf{k}'_+, \mathbf{k}', t)$ can be set into a form analogous to the Landau equation

$$\begin{aligned} &[\hbar\omega + E_L(\mathbf{k}) - E_{L'}(\mathbf{k}_+)] \delta n^{LL'}(\mathbf{k}) \\ &= [f_L(\mathbf{k}) - f_{L'}(\mathbf{k}_+)] q^{L'L}(\mathbf{k}_+, \mathbf{k}) V^{\text{ext}}(\mathbf{q}, \omega) \\ &\quad - i\hbar \text{Im}\{\Sigma_{\alpha}^{LL'}(\mathbf{k}, \omega)\} \delta \tilde{n}^{LL'}(\mathbf{k}), \end{aligned} \quad (\text{C3})$$

where $\delta \tilde{n}^{LL'}(\mathbf{k})$ is the contribution to $\delta n^{LL'}(\mathbf{k})$ which is proportional to $J_{\alpha}^{L'L}(\mathbf{k})$ and

$$\begin{aligned} \hbar \Sigma_{\alpha}^{LL'}(\mathbf{k}, \omega) &\approx - \sum_{\mathbf{q}'} |V_1(\mathbf{q}')|^2 \frac{1}{\hbar} [\mathcal{D}_0^{LL'}(\mathbf{k}, \mathbf{k}_+ + \mathbf{q}', \omega) \\ &\quad + \mathcal{D}_0^{LL'}(\mathbf{k} + \mathbf{q}', \mathbf{k}_+, \omega)] \left(1 - \frac{J_{\alpha}^{L'L}(\mathbf{k} + \mathbf{q}')}{J_{\alpha}^{L'L}(\mathbf{k})}\right) \end{aligned} \quad (\text{C4})$$

is the electron-hole self-energy for the case $V_1^{LL}(\mathbf{q}') \approx V_1(\mathbf{q}')$, and

$$\frac{1}{\hbar} \mathcal{D}_0^{LL'}(\mathbf{k}, \mathbf{k}', \omega) = \frac{1}{\hbar\omega + E_L(\mathbf{k}) - E_{L'}(\mathbf{k}') + i\hbar\eta}. \quad (\text{C5})$$

In expression (C3) the fact that the real part of the electron-hole self-energy is negligible in the impurity scattering case is taken into account.

The total induced density $\delta n^{LL'}(\mathbf{k})$ consists of the induced charge and current densities [denoted by $\delta n_0^{LL'}(\mathbf{k})$ and $\delta n_1^{LL'}(\mathbf{k})$ [40]], which are connected by the continuity equation $\hbar\omega \delta n_0^{LL'}(\mathbf{k}) + E_{LL'}(\mathbf{k}, \mathbf{k}_+) \delta n_1^{LL'}(\mathbf{k}) = 0$. The solution of the Landau equation (C3), together with the definition for the total optical conductivity

$$j_{\alpha}^{\text{ind}}(\omega) = \frac{1}{v} \sum_{LL'k\sigma} J_{\alpha}^{LL'}(\mathbf{k}) \delta n_1^{LL'}(\mathbf{k}) = \sigma_{\alpha\alpha}(\omega) E_{\alpha}^{\text{ext}}(\omega) \quad (\text{C6})$$

and with the relation

$$q^{L'L}(\mathbf{k}_+, \mathbf{k}) V^{\text{ext}}(\mathbf{q}, \omega) \approx \frac{\hbar J_{\alpha}^{L'L}(\mathbf{k})}{E_{L'L}(\mathbf{k}_+, \mathbf{k})} iE_{\alpha}^{\text{ext}}(\omega), \quad (\text{C7})$$

[corresponding to Eq. (12) combined with the relation $q_{\alpha} V^{\text{ext}}(\mathbf{q}, \omega) = iE_{\alpha}^{\text{ext}}(\omega)$] gives

$$\begin{aligned} \sigma_{\alpha\alpha}(\omega) &= \frac{i}{\omega v} \sum_{LL'k\sigma} \left(\frac{\hbar\omega}{E_{L'L}(\mathbf{k}_+, \mathbf{k})} \right)^{n_{LL'}} |J_{\alpha}^{LL'}(\mathbf{k})|^2 \\ &\times \frac{f_L(\mathbf{k}) - f_{L'}(\mathbf{k}_+)}{\hbar\omega + i\hbar\Gamma_{\alpha}^{LL'}(\mathbf{k}, \omega) + E_{LL'}(\mathbf{k}, \mathbf{k}) - \frac{E_{L'L}^2(\mathbf{k}, \mathbf{k}_+)}{\hbar\omega}}. \end{aligned} \quad (\text{C8})$$

Here $n_{LL} = 1$ in the intraband channel, $n_{LL} = 2$ in the interband channel, $\Gamma_{\alpha}^{LL'}(\mathbf{k}, \omega) = \text{Im}\{\Sigma_{\alpha}^{LL'}(\mathbf{k}, \omega)\}$ and $E_{LL'}(\mathbf{k}, \mathbf{k}') = E_L(\mathbf{k}) - E_{L'}(\mathbf{k}')$. The related long-wavelength susceptibility and the dielectric function become

$$\begin{aligned} e^2 \chi_{1,1}(\mathbf{q}, \omega) &= - \sum_{\alpha} \frac{iq_{\alpha}^2}{\omega} \sigma_{\alpha\alpha}(\omega), \\ \varepsilon(\mathbf{q}, \omega) &= 1 + \frac{4\pi i}{\omega q^2} \sum_{\alpha} q_{\alpha}^2 \sigma_{\alpha\alpha}(\omega), \end{aligned} \quad (\text{C9})$$

with $\mathbf{q} = \sum_{\alpha} q_{\alpha} \hat{e}_{\alpha}$. The expressions (C8)–(C9) are the generalization of the well-known single-band Landau response functions [40]. Obviously, to obtain Eqs. (22)–(23) of the main text we have to include the contributions beyond the three-band model, as well, by adding $\varepsilon_{\infty}(\mathbf{q}, \omega) - 1$ to the above expression for $\varepsilon(\mathbf{q}, \omega)$.

[1] P.Y. Yu and M. Cardona, *Fundamentals of Semiconductors* (Springer, Berlin, 1996).

[2] S. Uchida, T. Ido, H. Takagi, T. Arima, Y. Tokura, and S. Tajima, Phys. Rev. B **43**, 7942 (1991).

[3] S.L. Cooper, D. Reznik, A. Kotz, M.A. Karlow, R. Liu, M.V. Klein, W.C. Lee, J. Giapintzakis, D.M. Ginsberg, B.W. Veal, and A.P. Paulikas, Phys. Rev. B **47**, 8233 (1993).

[4] D. Reznik, S.L. Cooper, M.V. Klein, W.C. Lee, D.M. Ginsberg, A.A. Maksimov, A.V. Puchkov, I.I. Tar-takovskii, and S-W. Cheong, Phys. Rev. B **48**, 7624 (1993).

[5] S. Sugai, S.I. Shamoto, and M. Sato, Phys. Rev. B **38**, 6436 (1988); S. Sugai and N. Hayamizu, J. Phys. Chem. Solids **62**, 177 (2001).

[6] S. Sugai and T. Hosokawa, Phys. Rev. Lett. **85**, 1112 (2000).

[7] M. Opel, R. Nemetschek, C. Hoffmann, R. Philipp, P. F. Müller, R. Hackl, I. Tütto, A. Erb, B. Revaz, E. Walker, H. Berger, and L. Forró, Phys. Rev. B **61**, 9752 (2000).

[8] L. Tassini, F. Venturini, Q.-M. Zhang, R. Hackl, N. Kikugawa, and T. Fujita, Phys. Rev. Lett. **95**, 117002 (2005).

[9] M.M. Qazilbash, A. Koitzsck, B.S. Dennis, A. Gozar, Hamza Balci, C.A. Kendziora, R.L. Greene, and B. Blumberg, cond-mat/0510098; A. Gozar, S. Komiya, Y. Ando, and B. Blumberg, cond-mat/0510191.

[10] T.P. Devereaux, D. Einzel, B. Stadlober, R. Hackl, D.H. Leach, and J.J. Neumeier, Phys. Rev. Lett. **72**, 396 (1994).

[11] H. Ding, T. Yokoya, J.C. Campuzano, T. Takahashi, M. Randeria, M.R. Norman, T. Mochiku, K. Kadowaki, and J. Giapintzakis, Nature **382**, 51 (1996).

[12] J.W. Loram, K.A. Mirza, J.R. Cooper, and J.T. Tallon, J. Phys. Chem. Solids **59**, 2091 (1998).

[13] J.G. Naeini, X.K. Chen, J.C. Irwin, M. Okuya, T. Kimura, and K. Kishio, Phys. Rev. B **59**, 9642 (1999).

[14] I. Mrkonjić and S. Barišić, Eur. Phys. J. B **34**, 69 (2003).

[15] T. Yoshida, X.J. Zhou, T. Sasagawa, W.L. Yang, P.V. Bogdanov, A. Lanzara, Z. Hussain, T. Mizokawa, A. Fujimori, H. Eisaki, Z.-X. Shen, T. Kakeshita, and S. Uchida, Phys. Rev. Lett. **91**, 027001 (2003).

[16] A.A. Abrikosov and V.M. Genkin, Zh. Eksp. Teor. Fiz. **65**, 842 (1973) [Sov. Phys. JETP **38**, 417 (1974)].

[17] A. Zawadowski and M. Cardona, Phys. Rev. B **42**, 10 732 (1990).

[18] H. Monien and A. Zawadowski, Phys. Rev. B **41**, 8798 (1990).

[19] A. Virosztek and J. Ruvalds, Phys. Rev. B **45**, 347 (1992); J. Ruvalds and A. Virosztek, Phys. Rev. B **43**, 5498 (1991).

[20] T.P. Devereaux, Phys. Rev. B **45**, 12 965 (1992).

[21] T.P. Devereaux and D. Einzel, Phys. Rev. B **51**, 16 336 (1995).

[22] T.P. Devereaux, A. Virosztek, and A. Zawadowski, Phys. Rev. B **54**, 12 523 (1996).

[23] H. Nikšić, E. Tutiš, and S. Barišić, Physica C **241**, 247 (1995).

[24] D. Einzel and D. Maske, Phys. Rev. B **70**, 172507 (2004).

[25] I. Kupčić, Physica C **391**, 251 (2003).

[26] I. Kupčić and S. Barišić, Fizika A **14**, 47 (2005) [cond-mat/0506482].

[27] M.V. Klein and S.B. Dierker, Phys. Rev. B **29**, 4976 (1984).

[28] S. Barišić, I. Kupčić, and I. Batistić, Int. J. Mod. Phys. B **3**, 2051 (1989).

[29] S. Barišić and E. Tutiš, Solid State Commun. **87**, 557 (1993).

[30] E.Ya. Sherman and C. Ambrosch-Draxl, Solid State Commun. **115**, 669 (2000); E.Ya. Sherman, C. Ambrosch-Draxl, and O.V. Misochko, Phys. Rev. B **65**, 140510 (2002).

[31] J. Friedel and M. Kohmoto, Eur. Phys. J. B **30**, 427 (2002).

[32] S. Uchida and H. Takagi, Physica C **162-164**, 1677 (1989).

[33] V.J. Emery, Phys. Rev. Lett. **58**, 2794 (1987).

[34] G. Kotliar, P.A. Lee, and N. Read, Physica C **153-155**, 538 (1988); G. Kotliar, in: *Correlated Electron Systems*, edited by V.J. Emery (World Scientific, Singapore, 1992), p. 118.

[35] M. Grilli, G. Kotliar, and A.J. Millis, Phys. Rev. B **42**, 329 (1990).

[36] I. Kupčić, Phys. Rev. B **61**, 6994 (2000).

[37] D.K. Sunko and S. Barišić, Eur. Phys. J. B **46**, 269 (2005).

[38] A.A. Abrikosov, L.P. Gorkov, and I.E. Dzyaloshinski, *Methods of Quantum Field Theory in Statistical Physics* (Dover Publications, New York, 1975).

[39] G. D. Mahan, *Many-particle Physics* (Plenum Press, New York, 1990).

[40] D. Pines and P. Nozières, *The Theory of Quantum Liquids I* (Addison-Wesley, New York, 1989).

[41] I. Kupčić, Physica B **322**, 154 (2002); I. Kupčić, Physica B **344**, 27 (2004).

[42] S. L. Adler, Phys. Rev. **126** (1962) 413; N. Wieser, Phys. Rev. **129** (1962) 63.

[43] P. Županović, A. Bjeliš, and S. Barišić, Z. Phys. B **101**, 387 (1996).

[44] The present notations for the charge and current vertices, $eq^{L'L}(\mathbf{k}_+, \mathbf{k})$ and $J_\alpha^{L'L}(\mathbf{k})$, correspond to $e(\mathbf{k}L|\mathbf{k} + \mathbf{q}L')$ and $(e/m)(\mathbf{k}L|p_\alpha|\mathbf{k} + \mathbf{q}L')$ of the $\mathbf{q} \cdot \mathbf{p}$ perturbation theory. See, for example, F. Wooten, *Optical Properties of Solids* (Academic Press, 1972). But notice that here the charge and current vertices are obtained in the exact way, rather than perturbatively.

[45] S. Barišić and J. Zelenko, Solid State Commun. **74**, 367 (1990); S. Barišić, Int. J. Mod. Phys. B **5**, 2439 (1991).

[46] E.Ya. Sherman and C. Ambrosch-Draxl, Phys. Rev. B **62**, 9713 (2000).

[47] M.A. Quijada, D.B. Tanner, F.C. Chou, D.C. Johnston, and S.-W. Cheong, Phys. Rev. B **52**, 15 485 (1995).

[48] S. Lupi, P. Calvani, M. Capizzi, and P. Roy, Phys. Rev. B **62**, 12 418 (2000).

[49] F. Venturini, Q.-M. Zhang, R. Hackl, A. Lucarelli, S. Lupi, M. Ortolani, P. Calvani, N. Kikugawa, and T. Fujita, Phys. Rev. B **66**, 060502 (2002).

[50] I. Kupčić, S. Barišić, and E. Tutiš, Phys. Rev. B **57**, 8590 (1998).

[51] A. Schwartz, M. Dressel, G. Grüner, V. Vescoli, L. De-giorgi, and T. Giamarchi, Phys. Rev. B **58**, 1261 (1998).

[52] M.R. Norman, M. Randeria, H. Ding, and J.C. Campuzano, Phys. Rev. B **52**, 615 (1995).

- [53] M.C. Schabel, C.-H. Park, A. Matsuura, Z.-X. Shen, D.A. Bonn, Ruixing Liang, and W.N. Hardy, Phys. Rev. B **57**, 6090 (1998).
- [54] J.M. Ziman, *Electrons and Phonons* (Oxford University Press, London, 1972).
- [55] J.M. Ziman, *Principles of the Theory of Solids* (Cambridge University Press, London, 1979).
- [56] P.M. Platzman and P.A. Wolff, *Waves and Interactions in Solid State Plasmas* (Academic Press, New York, 1973).
- [57] H. Kontani, K. Kanki, and K. Ueda, Phys. Rev. B **59**, 14 723 (1999).